In-process Monitoring of Material Cross-Contamination Defects in Laser Powder Bed Fusion

Mohammad Montazeri[1], Reza Yavari[1], Prahalada Rao[1*], Paul Boulware[2]

[1] Mechanical and Materials Engineering Department,
University of Nebraska-Lincoln, Lincoln, Nebraska, 68516.
*Corresponding author, email: rao@unl.edu

[2] Edison Welding Institute (EWI), Columbus, Ohio, 43221.

Abstract

The goal of this work is to detect the onset of material cross-contamination in laser powder bed fusion (L-PBF) additive manufacturing (AM) process using data from *in situ* sensors. Material cross-contamination refers to trace foreign materials that may be introduced in the powder feedstock used in the process due to such reasons as, poor cleaning of the machine after previous builds, or inadequate quality control during production and storage of the powder. Material cross-contamination may lead to deleterious changes in the microstructure of the AM part and consequently affect its functional properties. Accordingly, the objective of this work is to develop and apply a spectral graph theoretic approach to detect the occurrence of material cross-contamination in real-time as the part is being built using in-process sensors. The central hypothesis is that transforming the process signals in the spectral graph domain leads to early and more accurate detection of material cross-contamination in L-PBF compared to the traditional delay-embedded Bon-Jenkins stochastic time series analysis techniques, such as autoregressive (AR) and autoregressive moving average (ARMA) modeling. To test this hypothesis, Inconel alloy 625 (UNS alloy 06625) test parts were made at Edison Welding Institute (EWI) on a custom-built L-PBF apparatus integrated with multiple sensors, including a silicon photodetector (with 300 nm to 1100 nm optical wavelength). During the process two types of foreign contaminant materials, namely, tungsten and aluminum particulates under varying degrees of severity were introduced. To detect cross-contamination in the part, the photodetector sensor signatures were monitored hatch-by-hatch in the form of spectral graph transform coefficients. These spectral graph coefficients are subsequently tracked on a Hotelling T^2 statistical control chart. Instances of Type II statistical error, i.e., probability of failing to detect the onset of material cross-contamination, was verified against X-ray computed tomography (XCT) scans of the part to be within 5% in the case of aluminum contaminant particles. In contrast, traditional stochastic time series modeling approaches, e.g., ARMA had corresponding Type II error exceeding 15%. Furthermore, the computation time for the spectral graph approach was found to be less than one millisecond, compared to nearly 100 milliseconds for the traditional time series models tested.

Keywords: Additive Manufacturing, Laser Powder Bed Fusion, Material Cross-Contamination, Real-time Monitoring.

List of abbreviations

AM	Additive Manufacturing
PBF	Powder Bed Fusion
L-PBF	Laser Powder Bed Fusion
EB-PBF	Electron Beam Powder Bed Fusion
DED	Directed Energy Deposition
XCT	X-ray Computed Tomography
UCL	Upper Control Limit
LCL	Lower Control Limit
AR	Autoregressive Time Series Model
ARMA	Autoregressive Moving Average Time Series Model
ARIMA	Autoregressive Integrative Moving Average Time Series Model

1. Introduction

1.1 Background and Motivation

Powder bed fusion (PBF) is an additive manufacturing (AM) process in which thermal energy from a focused source, such as a laser or electron beam, is used to selectively fuse regions of a powder bed [1]. Figure 1 shows a schematic of the PBF process. A layer of powder material is spread across a build plate (powder bed), and subsequently, certain areas of this layer of powder are melted (fused) with an energy source such as a laser or electron beam. The build plate is then lowered and another layer of powder is spread over it and melted [2]. This cycle continues layer-upon-layer until the part is built. The specific PBF process depicted in Figure 1 uses a laser power source for melting the material, accordingly, the convention is to refer to this technology as Laser Powder Bed Fusion (L-PBF). More than 50 input parameters including the feedstock material, scan strategy, input energy, part design, and machine environmental settings are known to influence the structure and physical properties of the part [3-5].

Please Insert Figure 1 Here.

Along with blown powder and wire-fed directed energy deposition (DED) technology, PBF is the AM process of choice for making metal parts. Recent studies in the aerospace industry have

demonstrated that the PBF process can drastically reduce the so-called *buy-to-fly* ratio, which is the ratio of the material that is required to make a part to the final weight of the part. The buy-to-fly ratio is typically 20:1 for traditional subtractive and formative processes, while in the case of metal AM this ratio can be as small as 2:1. Simultaneously, the lead time for delivering a new part design can be shortened from five months to less than a week [6-10]. This unprecedented flexibility in design and manufacturing offered by the advent of metal AM has the potential to revolutionize strategic industries, such as aerospace and biomedical.

Despite these possibilities, the poor consistency of AM parts hinders their wider adoption for making mission-critical components. Particularly, the presence of defects in AM parts, such as porosity and geometric distortion, deleteriously affect their functional properties, e.g., fatigue life and strength [11-13]. Given the layered nature of AM, defects may form at any layer and become permanently sealed in by subsequent layers if they are not detected and averted promptly. Hence, there is a need to monitor the integrity of each layer as it is being built to ensure compliance [13-15].

In the context of quality assurance in AM, the current practice is to examine the part after it is built using X-ray computed tomography (XCT), which is exceedingly expensive and cumbersome. In a recent review article, Seifi *et al.* [16] attest that given the small batch sizes and time required for production, statistical qualification of AM parts based on destructive materials testing may be prohibitively expensive and take over a decade to complete, and is therefore impractical.

However, if there exists a record to attest the integrity of every layer in terms of sensor data, and if this data can be correlated back to the XCT for a few test parts, then this recorded sensor data for each layer, instead of XCT scanning and destructive analysis, can be used to rapidly qualify the part quality. Thus, leading to a so-called *qualify-as-you-build* paradigm in AM [17,

18]. From the larger context of offline defect mitigation in L-PBF, current research in this area can be stratified into four main thrusts:

(1) Avoiding defects such as porosity or distortion, resulting from factors related to poor choice of process parameters, such as laser power and scan speed, through design of experiments-based optimization studies [19].

(2) Preventing build failures, such as re-coater crashes by careful calibration of the machine and avoiding malfunction of the optical train, e.g., cleaning and maintenance of the optical lens used for focusing the laser – which is inclined to become coated with residue from spatter and material vaporization, particularly, during long build cycles.

(3) Precluding build failures resulting from poor design of the part, e.g., steep overhang geometries, thin walls, overly fine features, ill-suited placement of support structures, and improper orientation of the part [5, 20-22].

(4) Maintaining the purity of the input feed stock, such as taking care to avoid material cross-contamination, in the form of organic, e.g., oil, grease, lubricants, hair, plastics, and glue, or inorganic wear debris or other powders ingredients in the feedstock powder. Such contamination of the powder has been shown to cause variation in the microstructure and functional properties of the part [23].

This work specifically focuses on point (4), viz., avoiding defects related to the contamination of the feedstock powder. The initiation of contamination-related defects in L-PBF can be traced to: (a) poor quality control of the material feedstock during its production and storage, and (b) inadequacies and lapses in the procedures used to purge trace material from the AM machine or powder recycling equipment after a build has been completed with a different material. Since, there are numerous opportunities for contaminants to manifest in any stage of the powder

production and powder handling aspects, it is important to detect the subtler process drifts due to presence of contaminants, so that opportune corrective action, such as re-melting a layer, can be instigated.

To put the challenge of cross-contamination in pictorial context, Figure 2 shows optical images of an etched Inconel 625 AM sample from this work contaminated with varying severities of tungsten and aluminum trace material. These images demonstrate that material cross-contamination changes the basic microstructure of the build, and has the proclivity to spread beyond the layer in which the contaminant particles are introduced. The following inferences can be drawn from this experimental result, which will be described further in depth in Sec. 3.

- Figure 2 (a): Contamination with tungsten manifests as unfused particles evident as light hued inclusions in the darker Inconel 625 matrix. This is probably because: (1) the melting point of tungsten is much higher (~ 3422 °C) than Inconel 625 (~1300 °C), and (2) tungsten is not an alloying element in Inconel 625. Given these two reasons tungsten does not dissolve into the Inconel 625 matrix. The contamination of Inconel with tungsten is a critical problem that may lead to premature failure of AM parts. For instance, in a recent publication, Brandão *et al*. hypothesize that given the hardness of tungsten, un-melted tungsten particles tend to become preferred sites for crack initiation under tensile loading [23].
- Figure 2 (b): Contamination with aluminum does not manifest in clearly distinguishable particle traces, however it tends to distort the meltpool. This because of two reasons:
  (1) Unlike tungsten, aluminum has a much lower melting point (~ 660 °C) than the melting point of Inconel 625 (~ 1300 °C). Further, aluminum is also an allowable alloying element in Inconel 625 (maximum 0.4% by mass). Hence, aluminum particles may dissolve into the Inconel 625 matrix.

(2) Aluminum particles may vaporize given the higher energy applied to melt Inconel 625. This vaporization of aluminum particles leads to uniform circular pores of diameter ~ 10 μm, which is termed as gas porosity or pinhole porosity in the literature [5].

Please Insert Figure 2 Here.

1.2 Objective and Hypothesis

As a first-step to realize the long-term aim of qualify-as-you-build in AM, the goal of this work is to detect the onset of material contamination-related anomalies in L-PBF. In pursuit of this goal, the objective is to develop and apply a spectral graph theoretic approach for real-time detection of material cross-contamination in-process signatures acquired by a photodetector sensor.

The central hypothesis is that tracking the signatures acquired from the photodetector in the spectral graph domain leads to early and more accurate detection of material cross-contamination in L-PBF, compared to the traditional Box-Jenkins stochastic delay-embedded time series analysis of the signal, such as autoregressive (AR) and autoregressive moving average (ARMA) modeling. This work addresses the following open research question in the context of material cross-contamination in L-PBF process – what process signatures can capture the onset of contamination?

The rest of this paper is organized is follows. The literature in the area of sensing and monitoring in AM is discussed in Sec. 2, followed by description of the experimental methodology to initiate controlled material cross-contamination in Sec. 3, the spectral graph theoretic approach is explained in Sec. 4, and subsequently applied to the L-PBF process signals in Sec. 5, followed by summary of the conclusions and avenues for future research in Sec. 6.

2. Status of the Related Research – Gaps and Challenges.

Brandão *et al*. report the effect of high density tungsten inclusions on the tensile strength and microstructure of L-PBF test parts [23]. Although, contaminants were found not to influence the mean tensile strength of the specimen, the fracture cracks during testing were found to initiate at the locations where contaminants were present. Furthermore, specimens with cross-contamination tended to have large variability in the tensile strength readings compared to those without contamination.

In the related context of purity and physical characteristics (diameter and shape) of the powder, studies have been conducted to understand the effect of powder reuse on part functional attributes in electron beam PBF (EB-PBF) [24]. This is because, unlike L-PBF, in EB-PBF the powder is maintained at a higher temperature [25]. Hence, there is a practical concern that repeated reuse of the powder in EB-PBF may lead to deviation in powder characteristics and hence the functional performance of the part. These studies have concluded that although the repeated reuse of the powder increases its oxygen content and changes it particle geometry, the impact of powder reuse on mechanical strength was statistically insignificant [24, 25].

The effect of feedstock characteristics on the mechanical properties of LPBF parts was investigated by Ardila *et al.* who found that the effect of reuse of Inconel 718 powder had statistically insignificant effect on material strength, nor did the shape of the powder particles deviate significantly over 14 iterations [26]. Recent studies by Clemon at University of California, Berkeley characterize the effect of powder properties on the process performance [27]. Thus the understanding of the effect of material cross-contamination on part microstructure in LPBF remains to be thoroughly investigated.

The second challenge that this work must tackle lies in the domain of data analytics and modeling in AM. The in-process sensor data in AM processes is heterogeneous (several different sensors are used), acquired at high velocity (the sampling rate of sensors is high), and the data is high in volume (several gigabytes of data are acquired for a build). There is an active and ongoing effort to develop data analytics and modeling approaches to track and monitor these sensor data in real-time, and relate the sensor signatures to functional properties [28, 29]. The need for approaches to synthesize the data gathered in AM processes has been explicitly designated as a research priority area in recent roadmap reports [30, 31].

Comprehensive review articles for in-process sensing are available in Ref. [28, 29, 32-35]. Significant research in the area is being done in academe [36], national laboratories, and industry [37-45]. Nassar and Reutzel, *et al.* at Pennsylvania State University experimented with imaging of the L-PBF powder bed under various illumination conditions [46]. Defects, such as large voids caused by improper raking of the powder across the bed were identified from these images [42, 43, 47]. They have also used a multispectral photodetector setup that concentrates on observing the line-to-continuum ratio of the laser plume in both the L-PBF and DED processes to detect the onset of defects, such as porosity [48, 49]. Lane *et al.* at NIST integrated an L-PBF machine (EOS M270) with thermal and high-speed cameras, and a photodetector [37]. Researchers at NIST are currently building a customized L-PBF testbeds instrumented with multiple sensors, based on findings at Edison Welding Institute (EWI) [44, 45]. A large body of work in sensing and monitoring in L-PBF is reported by the Kruth group [50-54] and Witt group [55-58] in Europe. The sensing and monitoring approaches for PBF used in these pioneering works are categorized into the following two broad areas:

- **Meltpool monitoring**: Optical cameras, high-speed cameras, Infrared (IR) cameras, photodetectors, and pyrometers are used to gage thermal, intensity, and morphological aspects of the meltpool. The visual systems and sensors are either embedded coaxially with the laser; or a system that is either external or internal to the chamber inclined at an angle to the build platen [28, 29]. The challenge is that the temperature profiles captured by IR systems is a trend and not the actual temperature. This is because the material emissivity has to be factored into the readings, and furthermore, if the sensor is mounted at an angle to the powder bed, the incident thermal radiation is therefore not perpendicular to the sensing elements in the IR camera, and which in turn affects the accuracy of the temperature reading.
- **Powder bed monitoring:** Acoustic (ultrasonic) sensors, vibration (accelerometers), optical cameras, and IR thermal cameras have also been proposed to monitor the powder bed conditions. For instance, Rieder *et al.* built a system with ultrasonic sensors mounted underneath the build platen to detect voids in the build [59]. Vibration sensors were used by Craeghs *et al.* to identify faulty deposition of powder layers resulting from a damaged recoater [54]. Instances of super elevations, poor surface finish, and defective features have been detected using both visual and vibration sensors. In a similar vein, Nassar *et al.* used optical images taken layer-by-layer to detect improper raking of the material and distortion during the process [42].

The work reported by Craeghs *et al.* in Ref. [54] serves as an archetypical example of both meltpool and powder bed monitoring. Craeghs *et al.* [54] incorporated three sensors, namely, a visual camera to ascertain the characteristics of the powder raked by the blade across the build platen, i.e., a powder bed monitoring system; and a photodiode (photodetector) and a camera

coaxially aligned with the laser, both of which are used to monitor the meltpool. In the context of monitoring the powder bed raked across the platen, Craeghs *et al.* made two observations. First, the gradual wear of the recoater blade causes streaks to appear across the deposited powder bed. In a similar vein, Abdelrahman *et al.* showed that non-uniform raking of the powder bed may lead to defects [43]. The effect of using a damaged recoater blade leads to discernable streaks on the powder bed surface, which in turn manifest in poor part surface finish. The uneven deposition of the material resulting from a damaged recoater blade was detected by Craeghs *et al.* using a statistical control chart-type strategy. The gray scale values of the powder bed taken by the visual camera are tracked and used as a feature to discriminate the onset of defects due to improper raking of the powder across the bed. For instance, the grayscale image values for a layer deposited with a damaged blade shows clear spikes compared to when the powder is raked uniformly.

Furthermore, the meltpool was monitored with the photodiode and optical camera system. The optical systems were augmented with filters to constrain the wavelength of acquired light in the region of 780 nm to 950 nm. The sampling rate of the photodiode is 10 kHz, this translates to a sample every 100 μm of the linear distance traversed by the laser, considering that the laser scan velocity is set at 1000 mm/sec. Incidentally, the laser scan velocity and sampling rate of the photodiode used by Craeghs *et al.* [54] is nearly identical to those in this work (see Sec. 3). Further, using image segmentation and pixel intensity estimation techniques from the area of image processing the authors track the meltpool area and the length to width ratio of the meltpool. These meltpool image features are the monitoring statistics which can be used in a statistical control chart; they have also shown to be indicative of process phenomena such as *balling* by other researchers [60, 61].

Another example is tendered by Craeghs *et al*. [54] for detecting porosity in L-PBF due to process drifts. In this case, abrupt machine errors led to increase in the part porosity. At certain instances, due to faults in the build platform stage motor, the powder bed was lowered farther than the set layer height. Hence, powder thickness equivalent to multiple layers was accidentally raked across the bed. This unusually high layer thickness led to increase in porosity, because, the energy applied per unit volume (volumetric energy density) was insufficient to melt the powder. The authors report that the photodiode signal depicts an inordinate increase in mean and standard deviation corresponding to layers with faulty deposition.

A lacuna of the analysis used in these prior works in sensing and modeling in AM, and as exemplified in the pioneering work of Craeghs *et al.* [54], is that they are largely offline and use approaches such as Fourier transforms or statistical-feature models, which as we will demonstrate in Sec. 5, are not amenable to online monitoring. To take these pioneering works in process monitoring in AM forward, it is necessary to develop approaches capable of detecting a wider variety of defects in real-time and with greater accuracy. Recent works by Yang *et al.*, [62] and Rao *et al.* [63] have attempted to overcome these challenges by resorting to advanced analytics, such as fractal signal analysis, and adaptive clustering and Bayesian modeling.

A drawback with these newer data analytics approaches is that they require well-defined model structures, e.g., logistic fractal model, tuning of parameters, setting the number of layers and nodes in a neural networks, and tuning the number of terms in traditional time series analysis techniques, such as ARMA. Furthermore, the classical time series approaches assume that the statistical moments of the signal do not change over time (stationarity assumption). These assumptions are not tenable in L-PBF, wherein the signal may not confirm with well-known

distributions, or may change from layer-to-layer and from a part design to the next. The spectral graph theoretic approach proposed herein has two advantages over existing approaches:

(1) The approach is feature-free, in that it does rely on extracting statistical features, such as mean or the frequency power spectrum to detect changes in the process; and

(2) It is model-free, i.e., it does not need an a priori defined model structure, such as number of time delay parameters as in stochastic time series modeling.

3. Experimental Setup and Sensor Data Acquisition

This section is divided into two parts. Sec. 3.1 describes the experimental setup and the procedure used to initiate contamination of different types and severity levels, and Sec. 3.2, which describes the sensor instrumentation and data acquisition methodology.

3.1 Experimental Setup and Procedure Used for Controlled Initiation of Contamination.

In this research, a customized, Open Architecture L-PBF Platform was designed and implemented at Edison Welding Institute (EWI) [45]. This platform, shown in Figure 3 (a and b) allows complete control of the key process factors, such as laser power, scan speed, scan pattern; commercial L-PBF systems typically do not allow users to customize the process settings. The energy source is a Ytterbium fiber laser with wavelength of 1070 nm operating in continious mode (manufacturer IPG). Furthermore, an array of heterogeneous sensors is integrated within the apparatus, and are located on an optical table near the laser scanning mechanism. Further details of this setup are available in Ref [45]. An Inconel 625 cuboid-shaped test part of size 10 mm × 10 mm × 15.20 mm (vertical build height) was made with the following parameters after extensive offline studies studies: scan velocity (V) 960 mm/s, laser power (P) 270 W, layer thickness (T) 0.040 mm, and hatch spacing (H) 0.1 mm, i.e., an applied volumetric energy density $E_V \approx 70$ J/mm^3 = P/(H×V×T). All powders used in this work are sourced from Electro Optical Systems GmbH

(EOS) and is commercially marketed as NickelAlloy IN625; in the material data sheet supplied by the company this material is stated as corresponding to UNS N06625 [64]. We note that the layer thickness of 0.040 mm is an input value to the system. It is controlled by accuracy of the motion stages on the build platform and the dispenser platform (typically 0.001 mm resolution). It is not an average of multiple layers or measured directly, but rather an input to the system and validated during preventive maintenance and calibration routines performed semi-annually.

To precisely control the degree of material contamination, a material dispensing setup was fabricated. The setup attaches to the recoater arm and powder material (contaminant) is dispensed from a motorized hopper. Figure 3 shows the schematic illustration of the sensor test bed and the equipment used for dispersion of the contaminants (tungsten and aluminum particles).

Please Insert Figure 3 Here.

The experimental procedure for dispersing contaminants, namely aluminum (Al) and tungsten (W), is depicted in Figure 4. The contaminants are dispersed over the powder bed every 20^{th} layer. This procedure for purposely introducing contamination was repeated 3 times over a total build consisting of 380 layers. The severity of contamination is controlled at three levels for each type of contaminant material, viz., aluminum and tungsten. Further, the contaminant particles are distributed over the powder bed in two ways, called dynamic contamination and static contamination. In the so-called static contamination, which occurs in levels labeled L_1, L_2, and L_3 (in ascending order of contaminant volume) the contaminant particles are dispensed entirely in one area of the layer and then raked across the bed. In the dynamic contamination mode, which occurs in layers labeled L_4, L_5 and L_6, the contaminant particles are dispensed continuously as the recoater moves across the bed.

The mechanism to initiate contamination is as follows. When the rotary dispenser shaft in Figure 3 (c) is started it opens the hopper and the contaminant material is dispensed through a

small notch from the hopper side to an open column. The contaminant particles are then deposited on the powder bed via a nozzle. There is a 0.5-mm gap between the nozzle that deposits the contaminants and the powder bed surface. The degree of contamination for every layer is controlled by varying the number of rotations of the dispenser shaft mechanism below the hopper. A relationship between the number of shaft rotations and the volume of material deposited was described in a patent application granted to EWI [65].

Please Insert Figure 4 Here.

In the static contamination mode, the recoater is stopped while it is raking the Inconel 625 powder and the shaft is rotated. This drops the contaminant onto one spot on the powder bed. The recoater then begins to move and spreads the contaminants on the powder bed. In the dynamic contamination mode, the contaminant powder is dispensed synchronous with the recoater movement. That is, the hopper motor in the fixture shown in Figure 3 (c) is continually operational as the recoater rakes the Inconel 625 powder across the bed. This sort of deposition of the contaminant results in an elongated line or streak across the powder bed, and is labeled L_4, L_5 and L_6 in ascending order of severity (Figure 5). The consequence of the different types of contamination modes, i.e., static and dynamic mode is captured using an in-process optical camera in Figure 5 (a1) and (a2); the severity of the contamination levels and their sequence within each replicate of experiment are further detailed in Figure 5 (b1) and (b2), and Table 1.

The quantifier used for assessing severity of contamination (Figure 5) is the volume contamination per unit area of the base material (Inconel 625), i.e., mm^3/mm^2. This measure accounts for the distribution profile of contaminant powder in each contamination level. As a result, length, width, and compactness of contaminant powder were considered in the design of the six levels of contamination (L_1, L_2 and L_3 for static contamination; and L_4, L_5 and L_6 for

dynamic contamination). There is the possibility of the contaminant powder accidentally leaking from the hopper if there are gaps in the mechanism assembly. If leakage were to occur it would lead to erroneous traceability – i.e., the in-process photodetector sensor signatures would (correctly) show a spike, while the layer would be (incorrectly) recorded by the operator as not been contaminated. To ensure that powder leakage does not occur during the experimental tests, the whole test bed including dispenser, build plate, and collector was sealed, and the hopper system is tested for 100 times. During these test runs, no leakage of powder is detected from the powder container on the build platform and collector.

Please Insert Figure 5a Here.
Please Insert Figure 5b Here.
Please Insert Table 1 Here

3.2 Sensor Integration and Procedure used for In-process Data Acquisition

Photodetector signal data is acquired for total of 10 following initiation of contamination as follows: (1) two layers prior to contamination, (2) the contaminated layer, and (3) seven layers subsequent to the contamination. In all, data is available for 180 of the total 380 layers of the build. The photodetector sensor is used in this study to detect occurrence of contamination. Specially, a Thorlabs model PDA36A photodetector is used and is located coaxial and synchronized with the switching of the laser, i.e., data is acquired only when the laser is active.

The analog photodetector signal is acquired via National Instruments NI 9215 analog input module. The detection range of the photodetector is the 350 nm to 1100 nm range with the gain of 40 dB, and the sampling rate is set at 10 KHz. The photodetector module is a Silicon junction photodiode (also called photoelectric pyrometer or photodiode) coupled with an amplifier, which proportionally translates radiated light intensity into an electrical signal. The transducing mechanism at play with this type of photodiode is the generation of a photocurrent upon light

absorption in the depleted region of the semi-conduction detecting element (silicon). The optical delivery to the photodetector aperture is integrated coaxially into the optical path of the laser, such that the light being interrogated stemmed from the laser plume during the melting process. In other words, the photodetector measures the radiation intensity of the laser plume (which in turn is proportional to the temperature of the meltpool) in terms of an amplified electrical signal with output in volts.

The sensor operates in a fast, highly linear manner, producing a current output proportional to light intensity absorbed by the sensor. The data is acquired hatch-by-hatch; the laser traces hatch pattern alternating manner as shown in Figure 6 – parallel (to the recoater direction) for odd layers, and perpendicular for even layers. The hatch pattern information will be used later in Sec. 5.2 to relate the sensor signatures to the position at which the contamination occurs in XCT. Each layer is comprised of 100 hatches, and each hatch takes ~ 0.01 sec. (10 milliseconds) to melt noting that the laser scan velocity is 960 mm/sec. Hence there are 100 photodetector data points acquired per hatch given that the sensor sampling rate is 10 KHz. In this build the laser stays on for ~ 1 sec. per layer, and for a total of under 7 minutes counting the time to melt the contour.

Please Insert Figure 6 Here.

4. The Spectral Graph Theoretic Approach

The aim of this section is to detect the onset of material cross-contamination in L-PBF process using in-process data. To realize this aim, the key idea is to transform the raw data into a domain that makes it tractable to extract signatures in real-time. In this work, the signal transformation procedure adopted is from the area of spectral graph theory, and has been discussed in depth in our previous research [66-71].

4.1 Overview of the Approach

A similar form as the approach proposed in this work has been used previously by the authors in the context of surface finish characterization in chemical mechanical planarization (CMP) semiconductor manufacturing process; monitoring chatter in ultraprecision diamond turning; and recently for assessment of post-process geometric integrity in polymer additive manufacturing [66-71]. The main difference of this work from these previous forays lies in the application of spectral graph eigenvectors for real-time classification of material cross-contamination in PBF. The previous works are mainly restricted for offline characterization, and use spectral graph eigenvalues which are not amenable for real-time adaptive monitoring of a fast-changing processes such as PBF. The underlying mathematics described herewith bears close resemblance to our previous works in spectral graph theory, but is nonetheless repeated here for the sake of cohesiveness and continuity [66-71].

The procedure is summarized in Figure 7, and encapsulates the four key steps. Steps 1 through 3 can be considered as the training phase, wherein a library of sensor signatures representing non-contaminated states is created. The last step, Step 4, classifies a hatch photodetector signal for each hatch into one of the two states, namely, contaminated vs. non-contaminated in real-time within a control chart framework. The underlying concept for each step is summarized herewith. The mathematical convention is to denote matrices and vectors with bold typesets.

Please Insert Figure 7 Here.

The approach has the following four steps, each of these steps is described in detail in the forthcoming section, Sec. 4.2.

Step 1: The photodetector signal $\boldsymbol{x}_l^p$ representing each hatch $p \in \{1 \dots h\}$ at layer $l \in \{1 \dots L\}$ of the melting process is converted into a weighted and undirected network graph $G \equiv (V, E, W)$. Where V, E and W are the graph vertices, edges and weight between the edges, respectively.

Step 2: The topological information in the graph $G \equiv (V, E, W)$ is extracted in terms of the eigenvectors ($\boldsymbol{v}_{\boldsymbol{x}_1^p}$) and eigenvalues ($\lambda_{\boldsymbol{x}_1^p}$) of the Laplacian matrix ($\boldsymbol{\mathcal{L}}_{\boldsymbol{x}_1^p}$). In other words, a spectral graph transform $G(\cdot)$ on the signal $\boldsymbol{x}_1^p$ is defined, i.e., $G(\boldsymbol{x}_1^p) \rightarrow \boldsymbol{\mathcal{L}}_{\boldsymbol{x}_1^p}(\lambda_{\boldsymbol{x}_1^p}, \boldsymbol{v}_{\boldsymbol{x}_1^p})$.

Step 3: A learning procedure is used to obtain a universal eigenvector basis $\boldsymbol{\mathcal{V}}_{normal}$ corresponding to the normal or non-contaminated process state. Through this universal basis a spectral graph Fourier transform $\hat{G}(\boldsymbol{x}_l^p) = \left[(\boldsymbol{x}_l^p)^T (\boldsymbol{\mathcal{V}}_{normal})\right]$ is defined for non-contaminated layers. Such a graph-based Fourier transform facilitates creating a library of spectral graph coefficients $\boldsymbol{C}$ archetypical of the non-contaminated process state.

Step 4: The coefficients $\boldsymbol{C}$ representative of the normal or non-contaminated process state are used to build a multivariate statistical control chart, called the Hotelling T^2 control chart. Given a new signal $\boldsymbol{y}$ an inner product with the basis vector $\boldsymbol{\mathcal{V}}_{normal}$, $\hat{G}(\boldsymbol{y}) = [(\boldsymbol{y})^T (\boldsymbol{\mathcal{V}}_{normal})]$, leads to a set of new spectral graph Fourier coefficients $\hat{G}(\boldsymbol{y})$ that are easily traced on the control chart. If $\hat{G}(\boldsymbol{y})$ falls outside the control limits established based on the data from the non-contaminated layers, then it is deemed as belonging to an out-of-control state, i.e., the data indicates that the layer is contaminated with trace materials.

4.2 Procedure for Applying Spectral Graph Theory to the L-PBF Photodetector data

Step 1: Converting the photodetector signal hatch-by-hatch into a network graph.

In this step, the aim is to represent each hatch related to the photodetector sensor data $\boldsymbol{x}$ as a weighted, undirected network $G(V, E, W)$. This graph $G(V, E, W)$ is a lower dimensional

representation of the signal $\boldsymbol{x}$. Consider a *m*-data point long 1-dimensional signal $\boldsymbol{x}$ for a layer $l \in \{1 \ldots L\}$ per the matrix shown in Eqn. (1).

$$\boldsymbol{x}_l = [x^1 \quad \ldots \quad x^i \quad \cdots \quad x^m]^{\mathrm{T}}, l \in \{1 \ldots L = 180\}. \tag{1}$$

In this work L = 180 (data from ten layers for each of the six levels of contamination replicated thrice, 10 × 6 × 3). Each layer is comprised of h hatches, in this work h = 100, m = 10,000. Thus, the signal $\boldsymbol{x}_l$ is further divisible into the corresponding h hatches, each hatch has k data points, with k = 100. This information was obtained by tracking the on-off switching time of the laser in each layer, i.e., the time between when the laser goes on and off relates to one hatch. Let each hatch in a layer be defined as a matrix $\boldsymbol{x}_l^p$ so that it can be written in matrix form as,

$$\begin{gathered}\boldsymbol{x}_l^p = \begin{bmatrix} x_l^1 & \ldots & x_l^q & \cdots & x_l^r & \cdots & x_l^k \end{bmatrix}^{\mathrm{T}}, \\ k \in \{1 \ldots k = 100\}, p \in \{1 \ldots h = 100\}, l \in \{1 \ldots L = 180\}.\end{gathered} \tag{2}$$

To transform a signal of each hatch into a network graph, the following procedure is followed. First, the pairwise comparisons w_{qr} is computed using a kernel function Ω [72] per Eqn. (3), where $x_l^{q,p}$ and $x_l^{r,p}$ are two points of the photodetector signal for a specific hatch $\boldsymbol{x}_l^p$

$$w_{qr}^{l,p} = \Omega\left(x_l^{q,p}, x_l^{r,p}\right) \forall\, q, r \in (1 \cdots k). \tag{3}$$

While different types of kernel functions Ω, such as the radial basis or Mahalanobis can be defined to obtain the graph G. For simplicity, in this work we use the standardized Euclidean kernel shown in Eqn. (4), where V is the variance of the one-dimensional signal $\boldsymbol{x}_l^p$.

$$w_{qr}^{l,p} = \left(x_l^{q,p} - x_l^{r,p}\right)\mathrm{V}^{-1}\left(x_l^{q,p} - x_l^{r,p}\right). \tag{4}$$

The symmetric *similarity matrix* $\boldsymbol{S}^{k\times k} = \left[w_{qr}^{l,p}\right]$ represents a weighted and undirected network graph G; each row and column of $\boldsymbol{S}$ is the vertex V (or node) of the graph, the relationship between two vertices is captured in terms of its connection status E and weight W. The graph is then represented as $G \equiv (V, E, W)$ [73]. To be more specific, we make the following notational additions to the similarity matrix $\boldsymbol{S}$ and graph G: $\boldsymbol{S}_{\boldsymbol{x}_l^p}$; $G_{\boldsymbol{x}_l^p}$, where $\boldsymbol{x}_l^p$ relates to a specific hatch p for the signal related to the layer *l*.

Notes for practical application: In practice, we found that the number of data points *k* in each hatch *h* may not be exactly 100, but may vary about 10%. As explained earlier, immediately following Eqn. (1), a hatch is readily demarcated in the data based on the laser activation time - when the laser goes off, the photodetector signal immediately degrades to zero as illustrated in Figure 12, Sec. 5.2. This method of demarcating a hatch is readily applicable in this work given the simple cuboid geometry of the test part (10 mm × 10 mm × 15.2 mm) – the hatch length, as shown in Figure 6, is constant across a layer. Such a regular and constant hatch length rarely occurs in practice.

Nevertheless, the approach can be readily modified even if a layer does not have a uniform hatch length. In case of an complex geometry a way to form the matrix $\boldsymbol{x}_l^p$ is by tracking the data over a fixed timeframe instead of a complete hatch. Moreover, the part geometry does not intrinsically affect the approach because a pairwise comparison between data points is taken in Eqn. (4) to track the change in the process.

Step 2: Extracting topological information for the graph surface

This phase aims to extract topological information from the graph G. Once the data $\boldsymbol{x}_l^p$ in a particular hatch is represented as a graph $G_{\boldsymbol{x}_l^p}$, the Laplacian Eigenvectors $\boldsymbol{v}_{\boldsymbol{x}_l^p}$ are computed. This

topological information is subsequently used to capture the process drifts from the nominal condition. From $\boldsymbol{S}_{\boldsymbol{x}_l^p}$, the *degree* $d_q^{l,p}$ of a node q, $q = \{1 \dots k\}$ is computed, which is a count of the number of edges that are incident upon the node. The node degree is the sum of each row in the similarity matrix $\boldsymbol{S}$. Subsequently, the diagonal *degree matrix* $\boldsymbol{\mathcal{D}}^{k\times k}$ is structured from $d_q^{l,p}$ as follows,

$$d_q^{l,p} = \sum_{r=1}^{k} w_{qr}^{l,p} \;\; \forall\, q = \{1 \dots k\}, \tag{5}$$

$$\boldsymbol{\mathcal{D}}^{k\times k} \stackrel{\text{def}}{=} \begin{bmatrix} d_1^{l,p} & \cdots 0 \cdots & 0 \\ \vdots & \ddots & \vdots \\ 0 & \cdots 0 \cdots & d_k^{l,p} \end{bmatrix}. \tag{6}$$

This leads to the normalized Laplacian $\boldsymbol{\mathcal{L}}$ of the graph G, for each hatch, which is defined as,

$$\boldsymbol{\mathcal{L}} \stackrel{\text{def}}{=} \boldsymbol{\mathcal{D}}^{-\frac{1}{2}} \times (\boldsymbol{\mathcal{D}} - \boldsymbol{S}) \times \boldsymbol{\mathcal{D}}^{-\frac{1}{2}},$$

$$\text{where, } \boldsymbol{\mathcal{D}}^{-\frac{1}{2}} = \begin{bmatrix} 1\Big/\sqrt{d_1^{l,p}} & \cdots 0 \cdots & 0 \\ \vdots & \ddots & \vdots \\ 0 & \cdots 0 \cdots & 1\Big/\sqrt{d_k^{l,p}} \end{bmatrix}. \tag{7}$$

Thereafter, the Eigen spectrum of $\boldsymbol{\mathcal{L}}$ is computed as,

$$\boldsymbol{\mathcal{L}}\boldsymbol{v} = \lambda \boldsymbol{v}. \tag{8}$$

At the end of step 2, we have essentially defined a spectral graph transform on a signal $\boldsymbol{x}_l^p$,

$$G\left(\boldsymbol{x}_l^p\right) \rightarrow \boldsymbol{\mathcal{L}}_{\boldsymbol{x}_l^p}(\lambda_{\boldsymbol{x}_l^p}, \boldsymbol{v}_{\boldsymbol{x}_l^p}). \tag{9}$$

In other words, we have transformed the signal $\boldsymbol{x}_l^p$ for a specific hatch in terms of the eigenvectors ($\boldsymbol{v}$) and eigenvalues ($\lambda_{\boldsymbol{x}_l^p}$) of its Laplacian matrix ($\boldsymbol{\mathcal{L}}_{\boldsymbol{x}_l^p}$).

Step 3: Building the signal basis and spectral transformation

This step aims to obtain the eigenvectors of $\boldsymbol{\mathcal{L}}_{\boldsymbol{x}_1^p}$ across all non-contaminated hatches and converge it towards a universal eigenvector basis. In other words, we want to represent the signal during the non-contaminated state in terms of a single or universal eigenvector represented as $\boldsymbol{\mathcal{V}}_{normal}$.

<u>*Step 3.1:*</u> A single universal basis $\boldsymbol{\mathcal{V}}_{normal}$ is obtained by applying a simple update schema. As the eigenvectors $\boldsymbol{v}_{\boldsymbol{x}_l^p}$, for each hatch is calculated, we update the basis as follows,

$$\begin{gathered}\boldsymbol{\mathcal{V}}_{\boldsymbol{x}_l^{p+1}} = \boldsymbol{\mathcal{V}}_{\boldsymbol{x}_l^p} + \Delta\left(\boldsymbol{v}_{\boldsymbol{x}_l^{p+1}} - \boldsymbol{v}_{\boldsymbol{x}_l^p}\right),\ p \in \{1 \dots h\}, l \in \{1 \dots L\}, \\ \boldsymbol{\mathcal{V}}_{normal} = \boldsymbol{\mathcal{V}}_{\boldsymbol{x}_L^h}\end{gathered} \tag{10}$$

Initialized with $\boldsymbol{\mathcal{V}}_{\boldsymbol{x}_1^1} = \boldsymbol{v}_{\boldsymbol{x}_1^1}$ with Δ set the to a small value (in our case 0.001). To make the process computationally simpler only a small set of the first 10 non-zero Eigenvectors of the Laplacian $\boldsymbol{\mathcal{L}}_{\boldsymbol{x}_1^p}$ are updated.

<u>*Step 3.2:*</u> We define the spectral graph transform, which is analogous to the discrete Fourier transform. A spectral graph Fourier transform $\hat{G}(\cdot)$ on a signal hatch $\boldsymbol{x}_l^p$ can be defined as follows [74-78],

$$\hat{G}\left(\boldsymbol{x}_l^p\right) = \left[\left(\boldsymbol{x}_l^p\right)^T(\boldsymbol{\mathcal{V}}_{normal}\ )\right], l = \{1 \dots L\}, p \in \{1 \dots h\} \tag{11}$$

Applying this inner product through all the non-contaminated layers and hatches by taking the product $\left(\boldsymbol{x}_l^p\right)^{\mathrm{T}} \cdot \boldsymbol{\mathcal{V}}_{normal}$, leads to the graph coefficient matrix $\boldsymbol{C}$.

$$\begin{gathered}\boldsymbol{C} = \left[\left[(\boldsymbol{x}_1^1)^T(\boldsymbol{\mathcal{V}}_{normal}\ ) = \boldsymbol{c}_{1,1}\right];\quad \cdots \quad ; \left[\left(\boldsymbol{x}_{\mathrm{L}}^p\right)^{\mathrm{T}}(\boldsymbol{\mathcal{V}}_{normal}\ ) = \boldsymbol{c}_{L,p}\right]\right] \\ l = \{1 \dots L\}, p \in \{1 \dots h\}\end{gathered} \tag{12}$$

Essentially, each term $\boldsymbol{c}_{l,p}$ is a matrix that is $1 \times n$ long, where n (= 10) is the number of Eigenvectors in the universal basis $\boldsymbol{V}_{normal}$ selected for analysis. Each $\boldsymbol{c}_{l,p}$ can be visualized as a set of output variables which needs to be tracked across the process – they are termed as spectral graph Fourier transform coefficients.

Step 4: Change point detection using spectral graph Hotelling T^2 control chart

This step aims to detect material cross-contamination by tracking the spectral graph transform coefficients $\boldsymbol{c}_{l,p}$. To realize this aim, we use a multivariate statistical control chart called the Hotelling T^2 [79]. The control limit of the chart is constructed based on the so-called *in-control state* which in the context of this work is defined as the non-contaminated signal. For the Hotelling T^2 control chart only the upper control limit (UCL) needs to be estimated as the lower control limit (LCL) is zero. The application of the control chart proceeds in two phases, in the first phase (Phase 1) called the training phase, the upper control limit of the chart is constructed based on the spectral graph Fourier coefficients from the non-contaminated state; and in the second phase (Phase 2), called the monitoring phase, the coefficients for incoming signals for each new hatch is tracked on the chart, and their status, i.e., whether they belong to contaminated or non-contaminated state is determined.

Step 4.1: Phase 1 – Training the control chart

In this phase we ascertain the control limits of the chart. Data points below the UCL are said to be *in-control*, which in the context of this work refers to non-contaminated state. The data points falling above the UCL are termed *out-of-control*. In this research, an out-of-control point is interpreted as the onset of cross-contamination.

For setting the control limits, we only use the photodetector signals from the two layers before the contamination is introduced, and only those from the first iteration of the build. Such an

exceedingly conservative strategy towards determining the control limits largely precludes the possibility of introducing signals which might be vitiated, noting that metallurgical analysis revealed that contamination tends to cascade over several subsequent layers (Figure 11). Accordingly, only 24 of the total 60 layers for which data is available in iteration 1 are used in the training phase, amounting to 2400 hatches. This translates to roughly 15% of the available data for 180 layers used for analysis.

The test statistic, or the point plotted on the control chart is called the T^2 value, and is delineated in Eqn. (13) where $\overline{\boldsymbol{C}}$ is the mean vector of spectral graph theoretic coefficients, and $\boldsymbol{\Sigma}^{-1}$ is the inverse of the covariance matrix of $\boldsymbol{C}$, and T is the transpose operator.

$$T_{l,p}^2 = \left(\boldsymbol{c}_{l,p} - \overline{\boldsymbol{C}}\right)^{\mathrm{T}} \boldsymbol{\Sigma}^{-1} \left(\boldsymbol{c}_{l,p} - \overline{\boldsymbol{C}}\right) \tag{13}$$

The upper control limit (UCL) of the chart is calculated using Eqn. (14) where $\beta_{\alpha,n/2,(hL-n-1)/2}$ is the upper α tail of a Beta distribution with parameters n (the number of eigenvectors = 10) and $h = 100$ and $L = 24$ are the number of hatches and number of layers, respectively. In this work, we set $\alpha = 0.0013$ for the Beta distribution as. The LCL of a Hotelling T^2 is set at zero with these parameter values, the Type I error rate is found to be within 10% irrespective of the type of contamination.

$$\mathrm{UCL} = \frac{(hL-1)^2}{hL} \beta_{\alpha,n/2,(hL-n-1)/2} \tag{14}$$

Thereafter, the T^2 values from Eqn. (13) are plotted on the control chart, and the UCL is revised by removing any data points that fall erroneously above it. The re-estimation of the control limit by removing erroneous out-of-control data is only done once, and is called the delete and revise procedure.

Step 4.2: Phase 2 – Using the control chart for monitoring the process

Once the UCL of a chart is determined, the new sensor signatures are plotted upon the chart as follows. Suppose a photodetector signal $\boldsymbol{y}$ is obtained for a hatch, we estimate its graph Fourier coefficients $\hat{G}(\boldsymbol{y})$ as,

$$\hat{G}(\boldsymbol{y}) = [(\boldsymbol{y})^{\mathrm{T}}(\boldsymbol{\mathcal{V}}_{normal})] \tag{15}$$

The Hotelling T^2 statistic, labeled T_y^2 for this new sensor signature is calculated as follows,

$$T_y^2 = \left(\hat{G}(\boldsymbol{y}) - \overline{\boldsymbol{C}}\right)^{\mathrm{T}} \boldsymbol{S}^{-1} \left(\hat{G}(\boldsymbol{y}) - \overline{\boldsymbol{C}}\right) \tag{16}$$

The T_y^2 value is plotted on the control chart, and if it falls above the UCL, we conclude that contamination has occurred.

We now briefly describe the statistical error measurements that underscore the effectiveness of detecting contamination in the context of a control chart. Control charts are culpable of two types of statistical errors, namely, Type I (α or false alarm) and Type II (β or failing to detect). The Type I error rate is the percentage of data points (each data point on the control chart used in this work represents a hatch) that are falsely categorized as falling above the upper control limit when the process is in-control. In other words, Type I error is a hatch that is falsely deemed to indicate contamination, i.e., there is no actual contamination, but the control chart erroneously indicates that contamination has occurred in that hatch.

The Type II (β) error rate is the percentage of data points that fall inside the UCL when they should in reality lie outside, i.e., contamination has occurred, but the control chart fails to indicate it because the data point falls inside the control limits. However, because it is not possible to pinpoint exactly which hatch is contaminated, but it is known beforehand which layer is

contaminated, accordingly, in this work we estimate the Type II error in terms of layers. The Type I and Type II error rates are estimated as follows:

$$\text{Type I error rate} = \alpha = \frac{\text{Number of hatches falsely indicated as belonging to contaminated layers}}{\text{Number of hatches expected in non} - \text{contamined layers}}$$

$$\text{Type II error rate} = \beta = \frac{\text{Number of layers incorrectly indicated as in control}}{\text{Number of contamined layers}}$$

There are two experimentally derived instances to verify these statistical detection errors:

1) Information from the experimental design, in that, we know the exact layers at which the contaminants are dispensed over the base powder.
2) The XCT scans of the part from which we can verify the presence of contamination on a layer when it is introduced. However, noting that the contamination is liable to spread from the layer in which it is introduced.to previous and subsequent layers.

5. Results and Discussion

5.1 Offline X-Ray Computed Tomography Analysis of the Build

build. Using XCT scans additionally allows verification of the online analysis. To realize this aim, the specimen is examined using XCT along the various cutting planes demarcated Figure 8. The XCT scanning was made at 225 kV with resulting voxel resolution of 16 μm and pixel pitch of 200 μm on a Perkin Elmer detector. The vertical and horizontal cross sections of the 3D volume captured for the tungsten contaminated specimen is shown in Figure 9, wherefrom the contaminant powder is clearly discerned.

Please Insert Figure 8 Here.

Figure 9 (a) shows the XCT across the vertical cross-section (Y-Z plane, cutting plane A-A as depicted in Figure 8) of the test artifact. Observed in Figure 9(a) are the contaminated layers over three replicates. Closer examination of these vertical cross-sections reveals that for high

tungsten contamination levels, such as L_3, the tungsten particles disperse up to three layers preceding the layer in which they are introduced, and as much as eight subsequent layers. In other words, contamination tends to cascade across layers, and influences the structure of both the preceding and subsequent deposition. This assertion is further corroborated through metallurgical analysis in Figure 11. Similarly, Figure 9(b) shows the effect of contamination as viewed along the X-Z direction (cutting plane B-B); Figure 9(c) is the cross-section taken along the X-Y direction (cutting plane C-C). We note that in Figure 9(a) and (b), due to procedural lapses during XCT scanning, the second level of tungsten contamination for the first iteration (L_2-1) was not captured. This missing data is demarcated by a star in Figure 9 (a) and (b). In the context of aluminum contamination, Figure 10 shows the vertical cross sections of the specimen; aluminum trace particles were not detected with XCT. To reiterate, aluminum contaminant particles are not discernable in the XCT images, because, (a) aluminum is an alloying element in Inconel 625, and (b) the melting point of aluminum (~ 660 °C) is much lower than the melting point of Inconel 625 (~ 1300 °C). Consequently, aluminum readily dissolves into the surrounding Inconel 625 matrix, and is therefore undetected in the XCT. Additionally, aluminum may also vaporize due to the high energy density (~ 70 J/mm^3) applied in the process to melt Inconel 625.

The specimen with embedded tungsten contaminant was sectioned and primary etched with an alcohol-based Kalling's solution. The specimens were secondary etched using a 10% wt. chromic acid solution at 2.4 volts. In the optical micrograph of the etched sample shown in Figure 11 (a) the presence of tungsten contaminants in the Inconel 625 matrix is evident. More remarkably, tungsten particle traces are observed not just in the layer they are introduced, but also over multiple layers – both preceding and subsequent layers. The spread of contaminants to layers beyond which they are introduced is hypothesized as the effect of the repeated remelting of the material.

However, modeling of the meltpool dynamics is required for confirming this effect. Recent computational modeling work at Lawrence Livermore National Laboratories by King *et al.* towards simulating the meltpool dynamics shows that material reflow and remelting influences the structure of the previous layers, and may even be used beneficially to control and mitigate defects, such as porosity [80-82]. Further investigation in this direction to elucidate how and why material contamination cascades across layers is beyond the scope of this work.

The cascading effect of contamination is further verified in the XCT observations in Figure 11(b). The XCT cross-section in Figure 11(b) is taken in the X-Y plane, the label *n* refers to the layer in which contamination is introduced, *n-1* is the immediate preceding layer, *n-2* is two layers prior, and so on. Similarly, a plus sign is used to indicate layers subsequent to layer *n*. The ensuing section, Sec. 5.2 applies a spectral graph theoretic approach to capture these instances of contamination during the build using data from the photodetector.

Please Insert Figure 9 Here. Please Insert Figure 10 Here. Please Insert Figure 11 Here.

5.2 Online Spectral graph Theoretic Analysis of the Signal to Detect Contamination

The photodetector signal related to the six level of tungsten and aluminum contamination for one iteration are shown in Figure 12(a) and (b), respectively. The layers contaminated with tungsten portray significant peaks. However, such a clear change is not apparent in the photodetector signal for the aluminum contamination case. We herewith provide a physical explanation of the signal characteristics.

Because the photodetector signal essentially captures the optical intensity of the plume during the melting process, it is reasoned that it is intimately related to the laser-material interaction. This effect has been observed by the AM research group at Penn State Applied Research Laboratory in

both LPBF and DED processes [48, 49]. In these pioneering works, researchers show that the photodetector signal is connected to the intrinsic microstructure of the part. In a similar vein, in this work, when the laser passes over the powder bed area having contaminant particles, the optical intensity of the vapor plume changes, which is captured by the photodetector, and hence it is related to the elemental material aspects. The justification for this reasoning is as follows.

A crucial difference between this work, and the research reported by the Penn State group is that the latter uses two photodiodes that capture two different wavelength intensities, one at 520 nm (called line emission spectrum) and 530 nm (called continuum spectrum) [48, 49]. The ratio of the two spectra (line to continuum ratio) has been shown in three successive works by this group to be strongly correlated to pore severity in both LPBF and DED, and hence can be deemed to capture the microstructure-level aspects.

In our present work, an unfiltered signal from a single photodiode is used. On juxtaposing the photodiode signal resulting from contamination from tungsten (Figure 12 (a)) with aluminum (Figure 12 (b)), it is evident that, when tungsten contamination occurs the amplitude of the signal (Volts) increases sharply from 1V to over 3V. Whereas for the case of aluminum contamination, barely any increase is evident. This observation that the photodiode voltage is dependent on the contaminant material, leads to the inference that the photodiode signal in this work is inclined to be element-specific.

Please Insert Figure 12 Here.

In this section, the proposed spectral graph theoretic algorithm is applied to the L-PBF process with the aim of detecting the onset of aluminum and tungsten cross-contamination from the photodetector signals. First, the photodetector signal for the non-contaminated state is apportioned hatch-by-hatch for each layer. This is possible because the laser position is tracked and recorded

throughout the build. The photodetector signal for each hatch p for layer l is denoted as $\boldsymbol{x}_l^p$ in Eqn. (2).

We note that there is no clear correlation evident in the amplitude of the signal and the severity of the signal – the statistical features of the signal could not discriminate between different types and levels of severity. Next, using Eqn. (3) and (4), the pairwise comparison between different rows of photodetector hatch is performed to provide the similarity matrix $\boldsymbol{S}$ related to graph $G \equiv (V, E, W)$. Going through the second step, the Laplacian matrix of graph $\boldsymbol{\mathcal{L}}$ is constructed using Eqn. (7). Then the first 10 (= n) non-zero Laplacian Eigenvectors $\boldsymbol{v}_i, i = \{2 \dots 11\}$ are used to build a spectral universal basis $\boldsymbol{\mathcal{V}}_{normal}$ necessary for spectral transformation (Eqn. (10)). Subsequently, the spectral graph Fourier coefficients ($\boldsymbol{C}$) are obtained by taking the inner product $\left(\boldsymbol{x}_l^p\right)^T(\boldsymbol{\mathcal{V}}_{normal})$ per Eqn. (12).

Finally, the coefficients are $\boldsymbol{C}$ are traced on a Hotelling T^2 control chart. Per the procedure for building the Phase 1 control chart described in Step 4.1, the UCL is first estimated by only considering the so-called in-control signal, viz., those layers not contaminated with tungsten or aluminum particles. As mentioned previously, this was restricted to 24 of the 60 layers for the first iteration of the build with approximately 100 hatches per layer. The T^2 statistic and UCL are calculated based on Eqn. (13) and (14).

The Phase 1 spectral graph theoretic Hotelling T^2 control chart along with the data for the six levels of tungsten and aluminum contamination for the first iteration is shown in Figure 13. There are a total of 6000 hatches (60 layers) for which the data is available in the first iteration. Each point of the control chart is representative of the spectral graph coefficients for one hatch. It is observed that the chart captures the occurrence of contamination almost instantaneously.

The Type I error is ≈ 1% for both tungsten and aluminum contamination in building the Phase 1 control chart. This Type 1 error is obtained after revising the control limit by removing the outliers (so-called delete and revise procedure applied only once). This manner of constructing the control limit is an extremely conservative strategy that prioritizes the Type I error rate over the Type II error rate. In other words, the Type I error for the control chart is maintained close to 1%, while the Type II error is estimated based on the results. Furthermore, the control limits for a type of contaminant material (tungsten or aluminum) remains fixed.

Please Insert Figure 13 Here.

Next, following the procedure in Step 4.2, the Hotelling T^2 chart is used to detect contamination in the rest of the two experimental iterations of the build. The data is representative of 120 layers, with each layer having 100 hatches for a total of 12,000 hatches. To plot the spectral control chart for the other replicates, the UCL stays identical from Phase 1 in Figure 13. As new data $\boldsymbol{y}$ arrives, it is multiplied with the universal basis $\boldsymbol{\mathcal{V}}_{normal}$ to extract the first ten spectral graph Fourier coefficients $\hat{G}(\boldsymbol{y})$ as shown in from Eqn. (15). Subsequently, T_y^2 is obtained in Eqn. (16), and plotted on the control chart. This simple inner product makes this approach suitable for online monitoring.

Figure 14 shows the application of the Phase 2 control chart to each type of contamination (tungsten and aluminum) over iteration 2 and 3, i.e., L_1-2 through L_6-2; and L_1-3 through L_6-3. Every level of tungsten contamination, both static and dynamic, is detected promptly by the control chart in Figure 14(a). Whereas, as evident in Figure 14(a), in the case of aluminum contamination, the contamination level L_5-3 (dynamic contamination type) is missed (an example of Type II error). This underscores some of the challenges with contamination detection.

Please Insert Figure 14 Here.

Table 2 summarizes the Type I and Type II errors estimated from three replicates of the experiment in detecting powder contamination. We note that because it is intractable to pinpoint *a priori* the exact hatch where contamination has occurred, the Type II errors are reported in terms of all the hatches for the entire layer where contaminants are added. In contrast, it is known for certain whether a hatch belongs to a non-contaminated layer, hence the Type I error can be localized with respect to every hatch.

Please Insert Table 2 Here.

5.3 Verification with Statistical Time Series Analysis

The results from the proposed approach are compared with traditional delay-embedded Box-Jenkins stochastic time series models, such as autoregressive (AR), autoregressive moving average (ARMA), and autoregressive integrative moving average (ARIMA) models [83]. Starting with the simplest model with two autoregressive terms, the model search is stopped when the number of terms in the model reaches 10. The stopping criteria is chosen so that the number of terms in the most complicated model does not exceed the number of eigenvectors (n =10) used in the spectral graph theoretic approach.

For instance, Eqn. (17), (18), and (19) show the AR(10), ARMA(6,4), and ARIMA(6, 4), respectively [83]. Where $\mathbb{L}$ is the lag operator, such that $\mathbb{L}^i(x_t) = x_{t-1}$, where x_t is a photodetector data point, i.e., amplitude of the photodetector signal at time *t*. The parameter α_i is connected to the AR part of the time series model, θ_i are the parameters of the moving average (MA) part and ε_t are model error terms. The terms α and θ are optimized using the time series modeling toolbox in Matlab, such that the sum of squared errors, i.e., $\sum_{\forall t} {\varepsilon_t}^2$ is minimized.

$$\text{AR(10) model: } (1 - \sum_{i=1}^{10} \alpha_i \, \mathbb{L}^i) x_t = \varepsilon_t \quad (17)$$

$$\text{ARMA(6,4) model: } (1 - \sum_{i=1}^{6} \alpha_i \, \mathbb{L}^i) x_t = (1 + \sum_{i=1}^{4} \theta_i \, \mathbb{L}^i) \varepsilon_t \quad (18)$$

ARIMA (6,4) model: $(1 - \sum_{i=1}^{6} \alpha_i \mathbb{L}^i)(1 - \mathrm{L})x_t = (1 + \sum_{i=1}^{4} \theta_i \mathbb{L}^i)\varepsilon_t$ (19)

In Phase 1, the model coefficients α and θ are trained to fit the data hatch-by-hatch (using Matlab), and then these model coefficients are tracked on a Hotelling T^2 control chart. The procedure followed is identical to the one described for the spectral graph theoretic approach previously in Sec. 5.2. The only difference is that α and θ are used to populate the library of coefficients $\boldsymbol{C}$ per Eqn. (12) instead of the spectral graph Fourier coefficients $\hat{G}(\boldsymbol{x}_l^p)$.

For each model, the Hotelling T^2 control chart is constructed and the Type I and Type II errors are estimated using the same procedure used for the proposed spectral graph theoretic approach. The Phase 2 results for the traditional stochastic time series methods are presented in Table 2, from which it is evident that the onset of material cross-contamination is promptly detected in the case of tungsten contamination; the Type II (β) error rate is negligible for tungsten contamination and the Type I (α) error is less than 1% for a majority of cases. However, detection of aluminum contamination is rather intractable with these existing traditional Box-Jenkins time series approaches; the Type II error exceeds 10%. These results are further juxtaposed with a Hotelling T^2 control chart built with statistical features extracted from each hatch, such as mean, standard deviation, skewness, etc. The results depicted in Table 2 also provide the average computation time for extracting the T^2 values for one hatch in the Phase 2 part of the control chart. We note that, the computation time for the proposed graph theoretic approach is less than a millisecond (~ 0.8 millisecond), which is magnitude smaller in comparison to traditional approaches. Thus attesting to the viability of the approach for real-time process monitoring in AM.

5.4 Consistency Between Spectral Graph Theory and XCT

Continuing with the analysis, since the position data for each hatch of the photodetector signal is available, the spectral graph T^2 coefficients can be correlated with the layer-by-layer

contamination pattern obtained from the XCT scan. Such an attempt is made in Figure 15 for the tungsten contamination case. In Figure 15(a), the Hotelling T^2 values for the spectral graph coefficients are color coded, with red indicating out-of-control or contaminated hatches. These color-coded T^2 values are superimposed on the XCT of the specimen taken along the X-Z cross-section in Figure 15(b); the XCT is along the cutting plane B-B in Figure 8. From the overlaid plot in Figure 15(b) it is evident that there is a near one-to-one correlation between the sensor signatures and the layer at which contamination occurs.

However, such an overlaid plot for the aluminum contamination case could not be produced, because, the XCT of Inconel 625 specimens contaminated with the aluminum particles did not show visually prominent inclusions (Figure 10). To reiterate, the XCT of parts with aluminum is not informative, because, (a) aluminum particles may dissolve within the Inconel 625 matrix given their low melting temperature relative to Inconel 625 (~ 660 °C vs. ~1300 °C), and (b) aluminum vaporizes due to the high energy density (70 J/mm^3) applied to process Inconel 625.

Please Insert Figure 15 Here.

This result corroborates that the spectral graph sensor signatures are indeed indicative of material cross-contamination and can be traced back to physical locations where contamination is present. This traceability of sensor signatures to XCT demonstrates the viability of the *qualify-as-you-build* paradigm in AM, wherein in-process sensor data instead of cumbersome offline measurement and testing can be used to rapidly qualify the part quality.

Furthermore, through this research, once the presence of contaminants is discovered at a layer, measures to forestall further their spread over future layers can be taken. Such a preventive strategy could be, for instance, rescanning an entire layer with higher energy density to ensure thorough fusion of contaminant particles like tungsten, or removing a layer using a hybrid additive-

subtractive strategy. This in-process *correct-as-you-build* strategy is possible with hybrid L-PBF systems, e.g., Matsuura Lumex Avance and Sodick OPM250L, which have an in-built subtractive machining attachment that can be used to remove a contamination-afflicted layer. In the worst-case scenario, the build can be stopped to prevent poor part quality and waste of expensive powder.

6. Conclusions and Future Work

This work describes a spectral graph theoretic approach to detect occurrence of material cross-contamination in laser powder bed fusion (L-PBF) additive manufacturing (AM) process based on in-process sensor data. The key idea is to convert a signal into its network graph equivalent, and subsequently, extract so-called spectral graph Fourier coefficients as surrogate signatures to track the process hatch-by-hatch. A photodetector signal is specifically used to demonstrate the efficacy of the approach of an L-PBF of an Inconel 625 alloy part. During the build, two types of foreign material contaminants are induced, namely, tungsten and aluminum varying in the severity and the controlled manner in which they are introduced – static deposition, and dynamic/continuous deposition over a layer.

The key advantages of the approach over existing time-delay stochastic time series modeling techniques, such as ARMA is that: (a) it does not require fitting a model to the data, essentially it is model-free; and (b) eschews decomposition or extraction of features from each incoming signal, a simple inner product with an eigenvector basis is required thus saving on computational time. As a result, the approach detects instances of material contamination with high accuracy; the worst case Type I error was found to be < ~1%, and Type II error < 5%, which presents a magnitude improvement over traditional time series modeling. The ability to detect contamination was corroborated with offline metallurgical and XCT scanning.

Specific conclusions from this work are as follows:

1. Metallurgical and XCT analysis of specimens revealed that contaminants are not confined to the layer in which they are introduced. Indeed, it was observed that contaminant particles not only enter previously deposited, but also tend to cascade to subsequent layers. The repeated re-melting of the material is hypothesized as the root cause of the behavior that leads to cascading of contamination to previous and subsequent layers. Physical modeling to explain the transportation of contaminant particles across layers is beyond the scope of this work.
2. Tungsten contamination is readily discernable in both offline metallurgical and XCT images, and online photodetector signals. This is probably because tungsten has a higher melting point and is also not elemental to Inconel 625. In contrast, aluminum has a lower melting point than Inconel 625 and may be present as an alloying in minor quantities (< 0.4%) in the same. There is also the possibility that aluminum may be vaporized during the build (which causes pinhole porosity). Therefore, contamination of Inconel 625 with aluminum is harder to discern in either the XCT or photodetector signals than the tungsten contamination case.
3. The graph Fourier coefficients were extracted for each hatch of the material and traced in a Hotelling T^2 control chart. The occurrence of both tungsten and aluminum contamination are detected with high fidelity using the spectral graph Fourier coefficients; the Type I and Type II errors are < ~1% and < 5%, respectively.
4. The Hotelling T^2 values obtained from the spectral graph theoretic Fourier coefficients are overlaid on the XCT scans of the specimen. A near one-to-one correlation is demonstrated between the status of the Hotelling T^2 values − whether they are in-control or out-of-control − and the layer at which contamination is observed in the XCT of the specimen.

A drawback of this work is that we have only used only a single type of sensor – a photodetector − to detect a specific type of defect, namely, material cross-contamination. The efficacy of the

approach using multiple sensors, such as a spectrometer and infrared thermal imaging for different types of defects remains to be ascertained. Furthermore, the material, i.e., whether the contamination relates to tungsten or aluminum, and the type of severity of contamination (L_1 through L_6, and static or dynamic) could not be classified based on data from a single photodetector. Lastly, the effect of contamination on the mechanical properties of the part needs to be quantified through materials testing. This will allow completing the loop between process phenomena, sensor signatures, and part properties. The authors will attempt to address these gaps in their future work in the area.

Acknowledgements

One of the authors (PKR) thanks the National Science Foundation for funding his work through Grant Nos. CMMI- 1719388, 1739696, and 175206. Specifically, the spectral graph theoretic approach for monitoring of complex signals was first proposed through the NSF grant CMMI-1719388. The further development and application of spectral graph theoretic signal processing to realize in-process defect isolation and correction in AM towards a *correct-as-you-build* paradigm was conceptualized and funded through CMMI-1752069 (CAREER). The authors also thank the three anonymous reviewers, and the associate editor of the journal – Dr. Z. J. Pei; their diligence, critical insights and constructive comments have gone a long way in reinforcing the rigor of this work.

References

[1] 2015, ASTM/ISO 52900-15: Standard Terminology for Additive Manufacturing, ASTM International,West Conshohocken, PA doi: 10.1520/ISOASTM52900-15

[2] Gibson, I., Rosen, D. W., and Stucker, B., 2010, Additive manufacturing technologies: rapid prototyping to direct digital manufacturing, Springer, New York. doi: 10.1007/978-1-4939-2113-3

[3] O'Regan, P., Prickett, P., Setchi, R., Hankins, G., and Jones, N., 2016, "Metal Based Additive Layer Manufacturing: Variations, Correlations and Process Control," Procedia Computer Science, **96**, pp. 216-224. doi: 10.1016/j.procs.2016.08.134

[4] DebRoy, T., Wei, H., Zuback, J., Mukherjee, T., Elmer, J., Milewski, J., Beese, A., Wilson-Heid, A., De, A., and Zhang, W., 2017, "Additive manufacturing of metallic components–process, structure and properties," Progress in Materials Science doi: 10.1016/j.pmatsci.2017.10.001

[5] Sames, W. J., List, F., Pannala, S., Dehoff, R. R., and Babu, S. S., 2016, "The metallurgy and processing science of metal additive manufacturing," International Materials Reviews, **61**(5), pp. 315-360. doi: 10.1080/09506608.2015.1116649

[6] Shinbara, T., 2013, "Additive manufacturing: Enabling advanced manufacturing," NAE Convocation of the Engineering Professional Societies, National Academy of Engineering, Washington, DC.

[7] Huang, R., Riddle, M., Graziano, D., Warren, J., Das, S., Nimbalkar, S., Cresko, J., and Masanet, E., 2016, "Energy and emissions saving potential of additive manufacturing: the case of lightweight aircraft components," Journal of Cleaner Production, **135**, pp. 1559-1570. doi: 10.1016/j.jclepro.2015.04.109

[8] Benny, T., Khoda, B., Rao, P., Sealy, M., and Zhou, C., 2017 (In-Press), "Chapter 14: Applications of Laser-based Additive Manufacturing," Laser-based Additive Manufacturing Processes, J. Usher, and L. Bian, eds., Springer.

[9] Badiru, A. B., Valencia, V. V., and Liu, D., 2017, Additive Manufacturing Handbook: Product Development for the Defense Industry, CRC Press, Florida. doi:

[10] Thompson, M. K., Moroni, G., Vaneker, T., Fadel, G., Campbell, R. I., Gibson, I., Bernard, A., Schulz, J., Graf, P., Ahuja, B., and Martina, F., 2016, "Design for Additive Manufacturing: Trends, opportunities, considerations, and constraints," CIRP Annals - Manufacturing Technology, **65**(2), pp. 737-760. doi: 10.1016/j.cirp.2016.05.004

[11] Lewandowski, J. J., and Seifi, M., 2016, "Metal additive manufacturing: a review of mechanical properties," Annual Review of Materials Research, **46**, pp. 151-186. doi: 10.1146/annurev-matsci-070115-032024

[12] Gorelik, M., 2017, "Additive manufacturing in the context of structural integrity," International Journal of Fatigue, **94**(2), pp. 168-177. doi: 10.1016/j.ijfatigue.2016.07.005

[13] Grasso, M., Laguzza, V., Semeraro, Q., and Colosimo, B. M., 2016, "In-Process Monitoring of Selective Laser Melting: Spatial Detection of Defects Via Image Data Analysis," ASME Transactions, Journal of Manufacturing Science and Engineering, **139**(5), pp. 051001-051001-051016. doi: 10.1115/1.4034715

[14] Sharratt, B. M., 2015, "Report prepared for the Defence Research and Development – Atlantic Research Centre, Canada: Non-destructive techniques and technologies for qualification of additive manufactured parts and processes. URL: http://cradpdf.drdc-rddc.gc.ca/PDFS/unc186/p801800_A1b.pdf," No. DRDC-RDDC-2015-C035, Sharratt Research and Consulting Inc. , Victoria, BC, Canada.

[15] Waller, J. M., Parker, B. H., Hodges, K. L., Burke, E. R., and Walker, J. L., 2014, " NASA/TM—2014–218560: Nondestructive Evaluation of Additive Manufacturing State-of-the-Discipline Report," National Aeronautics and Space Administration (NASA) Langley Research Center, Hampton, Virginia.

[16] Seifi, M., Salem, A., Beuth, J., Harrysson, O., and Lewandowski, J. J., 2016, "Overview of Materials Qualification Needs for Metal Additive Manufacturing," JOM, **68**(3), pp. 747-764. doi: 10.1007/s11837-015-1810-0

[17] Popova, E., Rodgers, T. M., Gong, X., Cecen, A., Madison, J. D., and Kalidindi, S. R., 2017, "Process-Structure Linkages Using a Data Science Approach: Application to Simulated Additive Manufacturing Data," Integrating Materials and Manufacturing Innovation, **6**(1), pp. 54-68. doi: 10.1007/s40192-017-0088-1

[18] Peralta, A. D., Enright, M., Megahed, M., Gong, J., Roybal, M., and Craig, J., 2016, "Towards rapid qualification of powder-bed laser additively manufactured parts," Integrating Materials and Manufacturing Innovation, pp. 1-23. doi: 10.1186/s40192-016-0052-5

[19] Teng, C., Gong, H., Szabo, A., Dilip, J. J. S., Ashby, K., Zhang, S., Patil, N., Pal, D., and Stucker, B., 2016, "Simulating Melt Pool Shape and Lack of Fusion Porosity for Selective Laser Melting of Cobalt Chromium Components," Journal of Manufacturing Science and Engineering, **139**(1), pp. 011009-011009-011011. doi: 10.1115/1.4034137

[20] Seifi, M., Gorelik, M., Waller, J., Hrabe, N., Shamsaei, N., Daniewicz, S., and Lewandowski, J. J., 2017, "Progress Towards Metal Additive Manufacturing Standardization to Support Qualification and Certification," JOM, **69**(3), pp. 439-455. doi: 10.1007/s11837-017-2265-2

[21] Bourell, D., Kruth, J. P., Leu, M., Levy, G., Rosen, D., Beese, A. M., and Clare, A., 2017 (In-Press), "Materials for additive manufacturing," CIRP Annals - Manufacturing Technology doi: 10.1016/j.cirp.2017.05.009

[22] Brika, S. E., Zhao, Y. F., Brochu, M., and Mezzetta, J., 2017, "Multi-Objective Build Orientation Optimization for Powder Bed Fusion by Laser," ASME Transactions, Journal of Manufacturing Science and Engineering, **139**(11), pp. 111011-111011-111019. doi: 10.1115/1.4037570

[23] Brandão, A., Gerard, R., Gumpinger, J., Beretta, S., Makaya, A., Pambaguian, L., and Ghidini, T., 2017, "Challenges in Additive Manufacturing of Space Parts: Powder Feedstock Cross-Contamination and Its Impact on End Products," Materials, **10**(5), p. 522. doi: 10.3390/ma10050522

[24] Tang, H. P., Qian, M., Liu, N., Zhang, X. Z., Yang, G. Y., and Wang, J., 2015, "Effect of Powder Reuse Times on Additive Manufacturing of Ti-6Al-4V by Selective Electron Beam Melting," JOM, **67**(3), pp. 555-563. doi: 10.1007/s11837-015-1300-4

[25] Slotwinski, J. A., Garboczi, E. J., Stutzman, P. E., Ferraris, C. F., Watson, S. S., and Peltz, M. A., 2014, "Characterization of Metal Powders Used for Additive Manufacturing," Journal of Research of the National Institute of Standards and Technology, **119**, pp. 460-493. doi: 10.6028/jres.119.018

[26] Ardila, L. C., Garciandia, F., González-Díaz, J. B., Álvarez, P., Echeverria, A., Petite, M. M., Deffley, R., and Ochoa, J., 2014, "Effect of IN718 Recycled Powder Reuse on Properties of Parts Manufactured by Means of Selective Laser Melting," Physics Procedia, **56**(Supplement C), pp. 99-107. doi: 10.1016/j.phpro.2014.08.152

[27] Clemon, L., 2017, "Material Quality and Process Monitoring in Metal Additive Manufacturing," University of California, Berkeley, Berkeley, CA.

[28] Mani, M., Lane, B., Donmez, A., Feng, S., Moylan, S., and Fesperman, R., 2015, "NISTIR 8036: Measurement Science Needs for Real-time Control of Additive Manufacturing Powder Bed Fusion Processes," NIST, Gaithersburg, MD.

[29] Mani, M., Lane, B. M., Donmez, M. A., Feng, S. C., and Moylan, S. P., 2017, "A review on measurement science needs for real-time control of additive manufacturing metal powder bed fusion processes," International Journal of Production Research, **55**(5), pp. 1400-1418. doi: 10.1080/00207543.2016.1223378

[30] 2013, "Measurement Science Roadmap for Metal-Based Additive Manufacturing - Report prepared by Energetics Corporation," National Institute of Standards and Technology, Gaithersburg, MD.

[31] Huang, Y., Leu, M. C., Mazumder, J., and Donmez, A., 2015, "Additive Manufacturing: Current State, Future Potential, Gaps and Needs, and Recommendations," Transactions of the ASME, Journal of Manufacturing Science and Engineering, **137**(1), p. 014001. doi: 10.1115/1.4028725

[32] Grasso, M., and Colosimo, B. M., 2017, "Process defects and in situ monitoring methods in metal powder bed fusion: a review," Measurement Science and Technology, **28**(4), p. 044005. doi: 10.1088/1361-6501/aa5c4f

[33] Tapia, G., and Elwany, A., 2014, "A Review on Process Monitoring and Control in Metal-Based Additive Manufacturing," Transactions of the ASME, Journal of Manufacturing Science and Engineering, **136**(6), p. 060801. doi: 10.1115/1.4028540

[34] Everton, S. K., Hirsch, M., Stravroulakis, P., Leach, R. K., and Clare, A. T., 2016, "Review of in-situ process monitoring and in-situ metrology for metal additive manufacturing," Materials & Design, **95**, pp. 431-445. doi: 10.1016/j.matdes.2016.01.099

[35] Spears, T. G., and Gold, S. A., 2016, "In-process sensing in selective laser melting (SLM) additive manufacturing," Integrating Materials and Manufacturing Innovation, **5**(1), p. 2. doi: 10.1186/s40192-016-0045-4

[36] Yao, B., Imani, F., and Yang, H., 2018, "Markov Decision Process for Image-guided Additive Manufacturing," IEEE Robotics and Automation Letters doi: 10.1109/LRA.2018.2839973

[37] Lane, B., Lane, B., Moylan, S., Moylan, S., Whitenton, E. P., Whitenton, E. P., Ma, L., and Ma, L., 2016, "Thermographic measurements of the commercial laser powder bed fusion process at NIST," Rapid prototyping journal, **22**(5), pp. 778-787. doi: 10.1108/RPJ-11-2015-0161

[38] Lane, B., Whitenton, E., and Moylan, S., "Multiple sensor detection of process phenomena in laser powder bed fusion," Proc. SPIE Commercial+ Scientific Sensing and Imaging, International Society for Optics and Photonics, pp. 986104-986104-986109.

[39] Reutzel, E., and Nassar, A., "A survey of sensing and control for metal-based additive manufacturing," Proc. Proceedings of the Solid Freeform Fabrication Conference.

[40] Nassar, A., Spurgeon, T., and Reutzel, E., "Sensing defects during directed-energy additive manufacturing of metal parts using optical emissions spectroscopy," Proc. Proceedings of the Solid Freeform Fabrication Symposium.

[41] Dunbar, A. J., Nassar, A. R., Reutzel, E. W., and Blecher, J. J., "A real-time communication architecture for metal powder bed fusion additive manufacturing," Proc. Proceedings of the Solid Freeform Fabrication Symposium, pp. 67-80.

[42] Foster, B., Reutzel, E., Nassar, A., Hall, B., Brown, S., and Dickman, C., "Optical, layerwise monitoring of powder bed fusion," Proc. Proceedings of the Solid Freeform Fabrication Symposium, pp. 295-307.

[43] Abdelrahman, M., Reutzel, E. W., Nassar, A. R., and Starr, T. L., 2017, "Flaw detection in powder bed fusion using optical imaging," Additive Manufacturing, **15**, pp. 1-11. doi: 10.1016/j.addma.2017.02.001

[44] Lane, B., Mekhontsev, S., Grantham, S., Vlasea, M., Whiting, J., Yeung, H., Fox, J., Zarobila, C., Neira, J., and McGlauflin, M., "Design, Developments, and Results from the NIST Additive Manufacturing Metrology Testbed (AMMT)," Proc. Proceedings of the Solid Freeform Fabrication Symposium, pp. 1145-1160.

[45] Boulware, P., 2016, "Final Technical Report to National Institute of Standards and Technology and National Center for Defense Manufacturing and Machining - Measurement Science Innovation Program for Additive Manufacturing: An Evaluation of In-Process Sensing Techniques Through the Use of an Open Architecture Laser Powder Bed Fusion Platform," No. NIST# 70NANB13H192 - 20140097, Edison Welding Institute (EWI), Cincinnati, OH.

[46] Nassar, A. R., Reutzel, E. W., Brown, S. W., Morgan, J. P., Morgan, J. P., Natale, D. J., Tutwiler, R. L., Feck, D. P., and Banks, J. C., "Sensing for directed energy deposition and powder bed fusion additive manufacturing at Penn State University," Proc. SPIE LASE, SPIE, p. 14.

[47] Chua, Z. Y., Ahn, I. H., and Moon, S. K., 2017, "Process monitoring and inspection systems in metal additive manufacturing: Status and applications," International Journal of Precision Engineering and Manufacturing-Green Technology, **4**(2), pp. 235-245. doi: 10.1007/s40684-017-0029-7

[48] Dunbar, A. J., and Nassar, A. R., 2018, "Assessment of optical emission analysis for in-process monitoring of powder bed fusion additive manufacturing," Virtual and Physical Prototyping, **13**(1), pp. 14-19. doi: 10.1080/17452759.2017.1392683

[49] Stutzman, C. B., Nassar, A. R., and Reutzel, E. W., 2018, "Multi-sensor investigations of optical emissions and their relations to directed energy deposition processes and quality," Additive Manufacturing, **21**, pp. 333-339. doi: 10.1016/j.addma.2018.03.017

[50] Berumen, S., Bechmann, F., Lindner, S., Kruth, J.-P., and Craeghs, T., 2010, "Quality control of laser- and powder bed-based Additive Manufacturing (AM) technologies," Physics Procedia, **5**, pp. 617-622. doi: 10.1016/j.phpro.2010.08.089

[51] Craeghs, T., Bechmann, F., Berumen, S., and Kruth, J.-P., 2010, "Feedback control of Layerwise Laser Melting using optical sensors," Physics Procedia, **5**, pp. 505-514. doi: 10.1016/j.phpro.2010.08.078

[52] Craeghs, T., Clijsters, S., Kruth, J. P., Bechmann, F., and Ebert, M. C., 2012, "Detection of Process Failures in Layerwise Laser Melting with Optical Process Monitoring," Physics Procedia, **39**, pp. 753-759. doi: 10.1016/j.phpro.2012.10.097

[53] Craeghs, T., Clijsters, S., Yasa, E., Bechmann, F., Berumen, S., and Kruth, J.-P., 2011, "Determination of geometrical factors in Layerwise Laser Melting using optical process monitoring," Optics and Lasers in Engineering, **49**(12), pp. 1440-1446. doi: 10.1016/j.optlaseng.2011.06.016

[54] Craeghs, T., Clijsters, S., Yasa, E., and Kruth, J.-P., "Online quality control of selective laser melting," Proc. Proceedings of the Solid Freeform Fabrication Symposium.

[55] Jacobsmuhlen, J. z., Kleszczynski, S., Schneider, D., and Witt, G., "High resolution imaging for inspection of Laser Beam Melting systems," Proc. IEEE International Instrumentation and Measurement Technology Conference, IEEE, pp. 707-712.

[56] Kleszczynski, S., zur Jacobsmühlen, J., Reinarz, B., Sehrt, J. T., Witt, G., and Merhof, D., "Improving process stability of laser beam melting systems," Proc. Fraunhofer Direct Digital Manufacturing Conference.

[57] Kleszczynski, S., Zur Jacobsmühlen, J., Sehrt, J., and Witt, G., "Error detection in laser beam melting systems by high resolution imaging," Proc. Proceedings of the Twenty Third Annual International Solid Freeform Fabrication Symposium.

[58] Wegner, A., and Witt, G., "Process monitoring in laser sintering using thermal imaging," Proc. Proceedings of the Solid Freeform Fabrication Conference pp. 8-10.

[59] Rieder, H., Alexander, D., Spies, M., Bamberg, J., and Hess, T., 2014 "Online Monitoring of Additive Manufacturing Processes Using Ultrasound," Proc. Proceedings of the European Conference on Non-Destructive Testing. October 6-10, 2014, Prague, Czech Republic.

[60] Gu, D., and Shen, Y., 2009, "Balling phenomena in direct laser sintering of stainless steel powder: Metallurgical mechanisms and control methods," Materials & Design, **30**(8), pp. 2903-2910. doi: 10.1016/j.matdes.2009.01.013

[61] Gusarov, A. V., Yadroitsev, I., Bertrand, P., and Smurov, I., 2007, "Heat transfer modelling and stability analysis of selective laser melting," Applied Surface Science, **254**(4), pp. 975-979. doi: 10.1016/j.apsusc.2007.08.074

[62] Yao, B., Imani, F., Sakpal, A. S., Reutzel, E. T., and Yang, H., 2017, "Multifractal Analysis of Image Profiles for the Characterization and Detection of Defects in Additive Manufacturing," Journal of Manufacturing Science and Engineering doi: 10.1115/1.4037891

[63] Roberson, D. A., Espalin, D., and Wicker, R. B., 2013, "3D printer selection: A decision-making evaluation and ranking model," Virtual and Physical Prototyping, **8**(3), pp. 201-212. doi: 10.1080/17452759.2013.830939

[64] 2018, "Materials for Metal Additive manufacturing Material Data Sheet: EOS NickelAlloy IN625," Electro Optical Systems GmbH (EOS), Munich, Germany.

[65] Jamshidinia, M., Boulware, P. C., Cronley, L., Marchal, J., and Mendoza, H., *Powder handling system for use in powder bed fusion additive manufacturing* Patent: US 20170341146A1. Dated 11/30/2017.

[66] Rao, P., Beyca, O., Bukkapatnam, S., Kong, Z. J., Case, K. E., and Komanduri, R., 2015, "A Graph Theoretic Approach for Quantification of Surface Morphology and its Application to

Chemical Mechanical Planarization (CMP) Process," IIE Transactions, **47**(10), pp. 1088-1111. doi: 10.1080/0740817X.2014.1001927

[67] Rao, P., Bukkapatnam, S., Kong, Z., Beyca, O., Case, K., and Komanduri, R., 2015, "Quantification of Ultraprecision Surface Morphology using an Algebraic Graph Theoretic Approach," Procedia Manufacturing, **1**, pp. 12-26. doi: 10.1016/j.promfg.2015.09.025

[68] Rao, P., Kong, Z., Kunc, V., Smith, R., Love, L., and Duty, C., 2015, "Assessment of Dimensional Integrity and Spatial Defect Localization in Additive Manufacturing (AM) using Spectral Graph Theory (SGT)," ASME Transactions, Journal of Manufacturing Science and Engineering, **138**, pp. 051007 -051019. doi: 10.1115/1.4031574

[69] Tootooni, M. S., Dsouza, A., Donovan, R., Rao, P. K., Kong, Z., and Borgesen, P., 2017, "Classifying the Dimensional Variation in Additive Manufactured Parts From Laser-Scanned Three-Dimensional Point Cloud Data Using Machine Learning Approaches," ASME Transactions, Journal of Manufacturing Science and Engineering, **139**(9), pp. 091005-091005-091014. doi: 10.1115/1.4036641

[70] Tootooni, M. S., Rao, P. K., Chou, C.-A., and Kong, Z. J., 2016, "A Spectral Graph Theoretic Approach for Monitoring Multivariate Time Series Data from Complex Dynamical Processes," IEEE Transactions Automation Science and Engineering, **Accepted - In Press** doi: 10.1109/TASE.2016.2598094

[71] Montazeri, M., and Rao, P., 2018, "Heterogeneous Sensor-based Build Condition Monitoring in Laser Powder Bed Fusion Additive Manufacturing Process using a Spectral Graph Theoretic Approach," Journal of Manufacturing Science and Engineering doi: 10.1115/1.4040264

[72] Shi, J., and Malik, J., 2000, "Normalized cuts and image segmentation," IEEE Transactions on Pattern Analysis and Machine Intelligence, **22**(8), pp. 888-905. doi: 10.1109/34.868688

[73] Chung, F. R. K., 1997, Spectral Graph Theory, American Mathematical Society, Providence, RI. doi:

[74] Sandryhaila, A., and Moura, J. M., 2013, "Discrete signal processing on graphs," IEEE transactions on signal processing, **61**, pp. 1644-1656. doi: 10.1109/TSP.2013.2238935

[75] Shuman, D. I., Narang, S. K., Frossard, P., Ortega, A., and Vandergheynst, P., 2013, "The emerging field of signal processing on graphs: Extending high-dimensional data analysis to networks and other irregular domains," IEEE Signal Processing Magazine, **30**(3), pp. 83-98. doi: 10.1109/MSP.2012.2235192

[76] Shuman, D. I., Ricaud, B., and Vandergheynst, P., "A windowed graph Fourier transform," Proc. IEEE Statistical Signal Processing Workshop (SSP), Ieee, pp. 133-136.

[77] Zhu, X., and Rabbat, M., "Graph spectral compressed sensing for sensor networks," Proc. IEEE International Conference on Acoustics, Speech and Signal Processing (ICASSP), IEEE, pp. 2865-2868.

[78] Lee, J. D., and Maggioni, M., "Multiscale analysis of time series of graphs," Proc. Proceedings of The 9th International Conference on Sampling Theory and Applications.

[79] Montgomery, D. C., 2009, Statistical quality control, Wiley New York. doi:

[80] Khairallah, S. A., Anderson, A. T., Rubenchik, A., and King, W. E., 2016, "Laser powder-bed fusion additive manufacturing: physics of complex melt flow and formation mechanisms

of pores, spatter, and denudation zones," Acta Materialia, **108**, pp. 36-45. doi: 10.1016/j.actamat.2016.02.014

[81] King, W., Anderson, A., Ferencz, R., Hodge, N., Kamath, C., and Khairallah, S., 2014, "Overview of modelling and simulation of metal powder-bed fusion process at Lawrence Livermore National Laboratory," Materials Science and Technology, **31**(8), pp. 957-968. doi: 10.1179/1743284714Y.0000000728

[82] King, W., Anderson, A., Ferencz, R., Hodge, N., Kamath, C., Khairallah, S., and Rubenchik, A., 2015, "Laser powder bed fusion additive manufacturing of metals; physics, computational, and materials challenges," Applied Physics Reviews, **2**(4), p. 041304. doi: 10.1063/1.4937809

[83] Hamilton, J. D., 1994, Time series analysis, Princeton university press Princeton, New Jersey. doi:

List of Tables

Table Number	Table Caption
Table 1	The build layout and contamination pattern. The contamination set of L_1 through L_6 was deposited three times, and in the end of 3 iterations was followed by 20 cover layers.
Table 2	The algorithm accuracy in comparison with traditional approaches for detecting the Tungsten and Aluminum contamination. The numbers in the parenthesis are from three-fold experimental replications.

Table 1: The build layout and contamination pattern. The contamination set of L_1 through L_6 was deposited three times, and in the end of 3 iterations was followed by 20 cover layers.

Contamination Set #	Base Line (BL) / Contamination Layer (L_n, n=1 to 6)	Start Layer	End Layer	End Height (mm)
Iteration 1	Base line (non-contaminated layer)	1	19	0.76
	(Static contamination) L_1 -1	20	20	0.80
	Base line (non-contaminated layer)	21	39	1.56
	(Static contamination) L_2 -1	40	40	1.60
	Base line (non-contaminated layer)	41	59	2.36
	(Static contamination) L_3 -1	60	60	2.40
	Base line (non-contaminated layer)	61	79	3.16
	(Dynamic contamination) L_4-1	80	80	3.20
	Base line (non-contaminated layer)	81	99	3.96
	(Dynamic contamination) L_5-1	100	100	4.00
	Base line (non-contaminated layer)	101	119	4.76
	(Dynamic contamination) L_6-1	120	120	4.80
× 2 iterations of the build pattern	BL- L_1-2 through L_6 -2 BL- L_1-3 through L_6 -3	121	360	14.44
Cover Layers	Base line (non-contaminated layer)	361	380	15.20

Table 2: The algorithm accuracy in comparison with traditional approaches for detecting the Tungsten and Aluminum contamination. The numbers in the parenthesis are from three-fold experimental replications.

		Aluminum Contamination		Tungsten Contamination		Computation time per hatch (sec)
Model	Model Structure	Type I error (%)	Type II error (%)	Type I error (%)	Type II error (%)	
ARMA	(2,2)	0.6 (0.1)	83.3 (0.0)	1.0 (0.1)	0.0 (0.0)	0.0912
	(2,4)	0.6 (0.1)	83.3 (0.0)	1.0 (0.1)	0.0 (0.0)	0.0971
	(2,6)	0.6 (0.1)	83.3 (0.0)	1.0 (0.0)	0.0 (0.0)	0.1021
	(4,2)	0.7 (0.1)	83.3 (0.0)	1.2 (0.1)	0.0 (0.0)	0.0968
	(4,4)	0.7 (0.1)	83.3 (0.0)	1.3 (0.2)	0.0 (0.0)	0.0976
	(4,6)	0.8 (0.2)	66.7 (16.7)	1.2 (0.0)	0.0 (0.0)	0.1302
	(6,2)	1.2 (0.1)	33.3 (17)	1.0 (0.1)	0.0 (0.0)	0.1588
	(6,4)	1.7 (0.1)	16.7 (9.2)	1.0 (0.1)	0.0 (0.0)	0.2829
ARIMA	(2,2)	0.6 (0.2)	83.3 (0.0)	0.8 (0.1)	0.0 (0.0)	0.1128
	(2,4)	0.5 (0.1)	83.3 (0.0)	0.9(0.1)	0.0 (0.0)	0.1216
	(2,6)	0.7 (0.2)	83.3 (0.0)	0.9 (0.0)	0.0 (0.0)	0.1225
	(4,2)	1.1 (0.1)	66.7 (16.7)	1.3 (0.0)	0.0 (0.0)	0.2164
	(4,4)	1.2 (0.0)	66.7 (16.7)	1.3 (0.10	0.0 (0.0)	0.2576
	(4,6)	1.1 (0.0)	66.7 (16.7)	1.2 (0.1)	0.0 (0.0)	0.1560
	(6,2)	1.5 (0.1)	11.1 (9.6)	1.6 (0.2)	0.0 (0.0)	0.2011
	(6,4)	1.6 (0.1)	11.1 (9.6)	1.6 (0.1)	0.0 (0.0)	2.4152
AR	(2)	1.0 (0.0)	22.2 (19.2)	1.0 (0.20	0.0 (0.0)	0.0210
	(4)	1.1 (0.1)	16.7 (9.2)	0.9 (0.3)	0.0 (0.0)	0.0089
	(6)	0.8 (0.2)	16.7 (9.6)	0.9 (0.1)	0.0 (0.0)	0.0080
	(8)	0.7 (0.10)	16.7 (9.6)	0.9 (0.1)	0.0 (0.0)	0.0085
	(10)	0.5 (0.1)	33.3 (17)	0.8 (0.2)	0.0 (0.0)	0.8641
Statistical Control Chart		1.5 (0.0)	11.1 (9.6)	1.3 (0.7)	0.0 (0.0)	0.0427
Proposed Spectral Graph Theoretic Approach		0.5 (0.0)	5.0 (9.2)	1.1 (0.1)	0.0 (0.0)	0.0008

List of Figures

Figure Number	Figure Caption
Figure 1	The schematic diagram of the L-PBF process.
Figure 2	Optical image of an etched and polished Inconel 625 specimen. The black arrow indicates the build direction. (a) Contamination with tungsten, which due to its high melting point does not fuse, and tends to cascade through several layers. The dashed-line (1) indicates the shape of a melt pool, penetrated into the previously deposited layer. Also, the overlaps between tracks could be recognized. The dashed line and circle (2) shown at the bottom of the tungsten specimen are representative of the hatching directions in the two consecutive layers. (b) The contamination with aluminum is not readily evident as trace particles, but closer examination of the hatch pattern reveals that aluminum tends to distort the meltpool as indicated by the arrows (3), and (4) vaporization of the aluminum particles causes uniform circular pinhole (gas-induced) porosity of diameter ~10 μm.
Figure 3	(a) A schematic representation of the open architecture L-PBF platform at EWI [45]. For scale purposes, the powder bed on the machine accommodates parts as large as 10 inch × 10 inch (250 mm × 250 mm). (b) Photograph of the L-PBF platform (c) Schematic of the fixture made to deliver metered amount of contamination. (d) Photograph of the actual apparatus made for initiating contamination [65].
Figure 4	The manner in which contamination is introduced during the build. The gray layers show the ones where data is captured. The red layers indicate where the contamination is introduced.
Figure 5a	Post recoating optical images after contamination with (a1) Tungsten and (a2) Aluminum.
Figure 5b	The unit volumes of deposited powders for each of six contamination levels in (b1) tungsten and (b2) aluminum.
Figure 6	The horizontal and vertical hatch patterns related to odd and even layers respectively. The symbols O and X demarcate the starting and ending points for a hatch. There are 100 hatches per layer, each hatch takes close to 10 milliseconds to melt (laser velocity 960 mm/sec), the entire layer takes ~ 1 sec. to fuse.
Figure 7	Graphical overview of the proposed spectral graph theoretic approach for detecting material contamination.
Figure 8	Three-dimensional (3D) reconstruction of the XCT scan for the specimen contaminated with tungsten powder particles. The powder recoating moves along the X-axis direction.

Figure 9	The cross sectional XCT views of the Inconel 625 specimen contaminated by the tungsten powder particles, (a) vertical cross section normal to the recoating direction (cutting plane A-A, Y-Z direction),(b) vertical cross section along the recoating direction (cutting plane B-B, X-Z direction) (c) horizontal cross section (cutting plane C-C, X-Y direction). Due to procedural lapses in the XCT process the second contamination level in the first iteration (L2-1) was missed.
Figure 10	The cross sectional views of the Inconel 625 specimen contaminated by the Aluminum powder particles, (a) vertical cross section normal to the recoating direction (cutting plane A-A, Y-Z direction), (b) vertical cross section along the recoating direction (cutting plane B-B, X-Z direction). The contaminant particles are not evident within the aluminum matrix.
Figure 11	(a)The optical micrograph of the Inconel 625 specimen contaminated with tungsten particles observed over 8 layers. (b)(c) XCT images in the horizontal plane section (cutting plane C-C, X-Y direction) for the L_3 severity level shows that trace tungsten particles persist over eight subsequent layers and penetrate through three preceding layers.
Figure 12	(top row) The photodetector signal associated with the six level of (a) Tungsten contamination and (b) Aluminum contamination in Inconel 625. (bottom row) The second contamination level (L_2) is magnified and the signal corresponding to tungsten contamination has clear spikes compared to aluminum.
Figure 13	The Phase 1 spectral Hotelling T^2 control chart related to six levels of contamination for (a) Tungsten and (b) Aluminum contamination, wherein the control limits are fixed.
Figure 14	The Phase 2 spectral Hotelling T^2 control chart applied to two replications of the data for the related to the remaining two iterations, for each of the six levels of contamination for (a) tungsten and (b) aluminum contamination. Note that the dynamic contamination case L_5 for aluminum is not detected, indicating a Type II statistical error.
Figure 15	(a) The T^2 values of the spectral graph Fourier coefficients are color coded, red indicates out-of-control (contaminated) hatches, and black indicates in-control hatches. These T^2 values are plotted along the X-Z plane of the part, since the position of each hatch is known. (b) The spectral graph T^2 values are overlaid upon the XCT scan to demarcate the near one-to-one correspondence between the two.

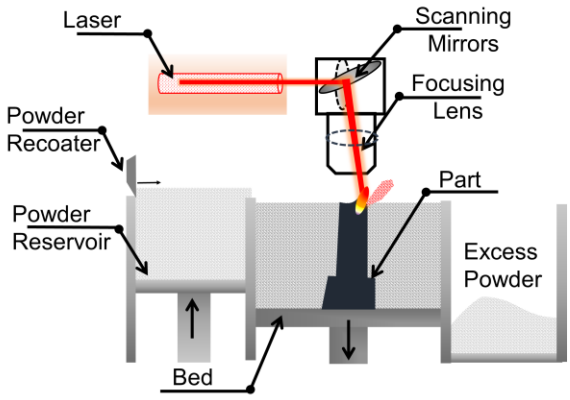

Figure 1: The schematic diagram of the L-PBF process.

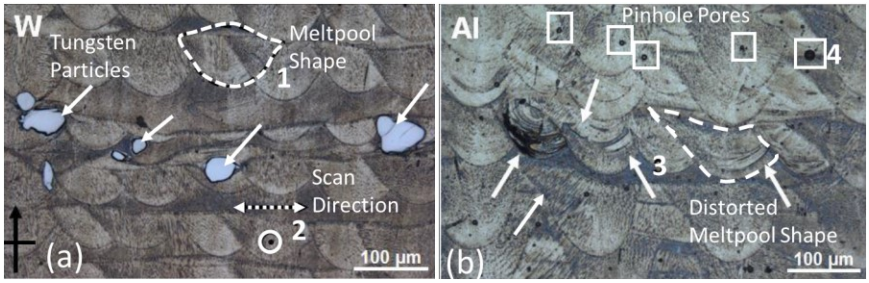

Figure 2: Optical image of an etched and polished Inconel 625 specimen. The black arrow indicates the build direction.

(a) Contamination with tungsten, which due to its high melting point does not fuse, and tends to cascade through several layers. The dashed-line (1) indicates the shape of a melt pool, penetrated into the previously deposited layer. Also, the overlaps between tracks could be recognized. The dashed line and circle (2) shown at the bottom of the tungsten specimen are representative of the hatching directions in the two consecutive layers.

(b) The contamination with aluminum is not readily evident as trace particles, but closer examination of the hatch pattern reveals that aluminum tends to distort the meltpool as indicated by the arrows (3), and (4) vaporization of the aluminum particles causes uniform circular pinhole (gas-induced) porosity of diameter ~10 µm.

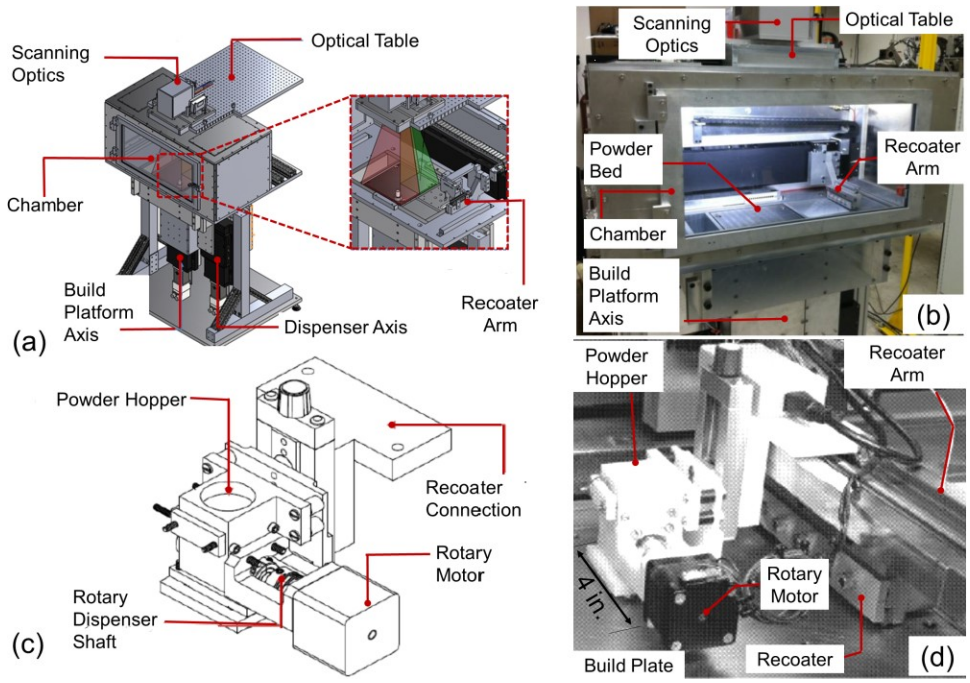

Figure 3: (a) A schematic representation of the open architecture L-PBF platform at EWI [45]. For scale purposes, the powder bed on the machine accommodates parts as large as 10 inch × 10 inch (250 mm × 250 mm). (b) Photograph of the L-PBF platform (c) Schematic of the fixture made to deliver metered amount of contamination. (d) Photograph of the actual apparatus made for initiating contamination [65].

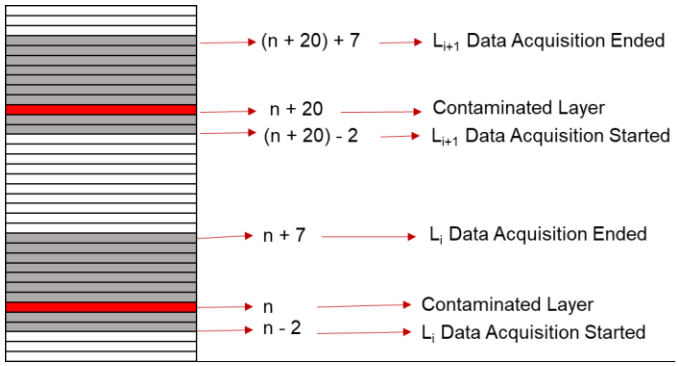

Figure 4: The manner in which contamination is introduced during the build. The gray layers show the ones where data is captured. The red layers indicate where the contamination is introduced.

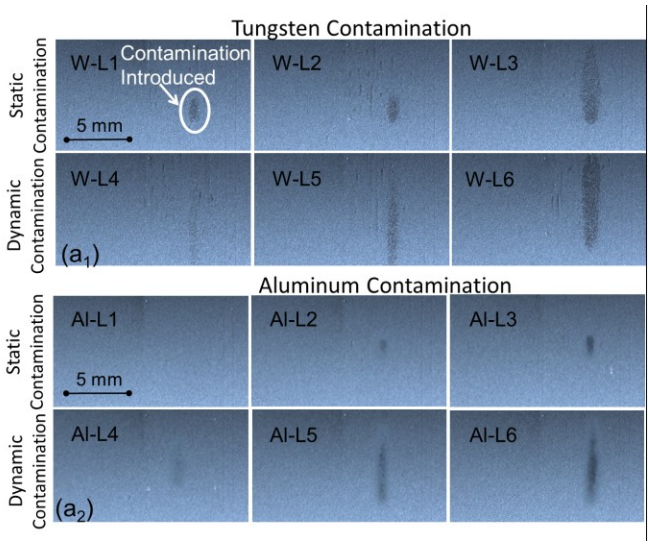

Figure 5

Figure 5a: Post recoating optical images after contamination with (a1) Tungsten and (a2) Aluminum.

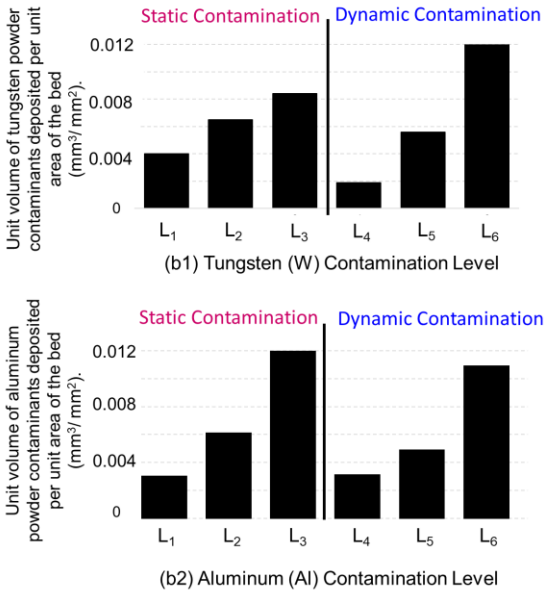

Figure 5b: The unit volumes of deposited powders for each of six contamination levels in (b1) tungsten and (b2) aluminum.

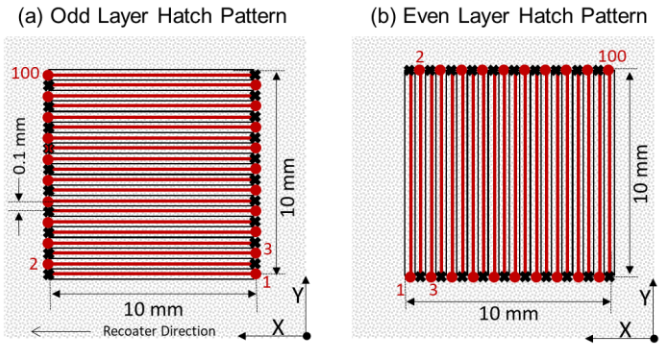

Figure 6: The horizontal and vertical hatch patterns related to odd and even layers respectively. The symbols O and X demarcate the starting and ending points for a hatch. There are 100 hatches per layer, each hatch takes close to 10 milliseconds to melt (laser velocity 960 mm/sec), the entire layer takes ~ 1 sec. to fuse.

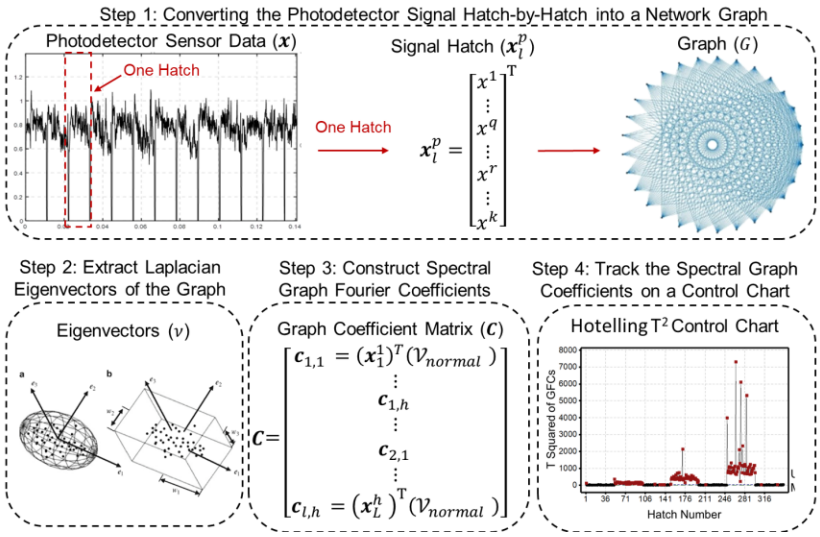

Figure 7: Graphical overview of the proposed spectral graph theoretic approach for detecting material contamination.

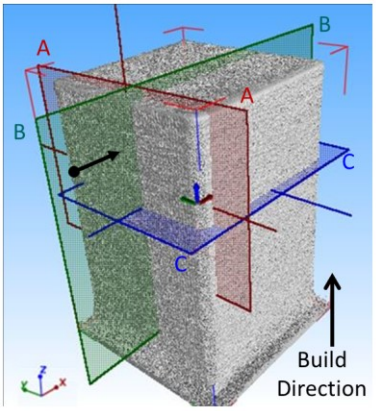

Figure 8: Three-dimensional (3D) reconstruction of the XCT scan for the specimen contaminated with tungsten powder particles. The powder recoating moves along the X-axis direction.

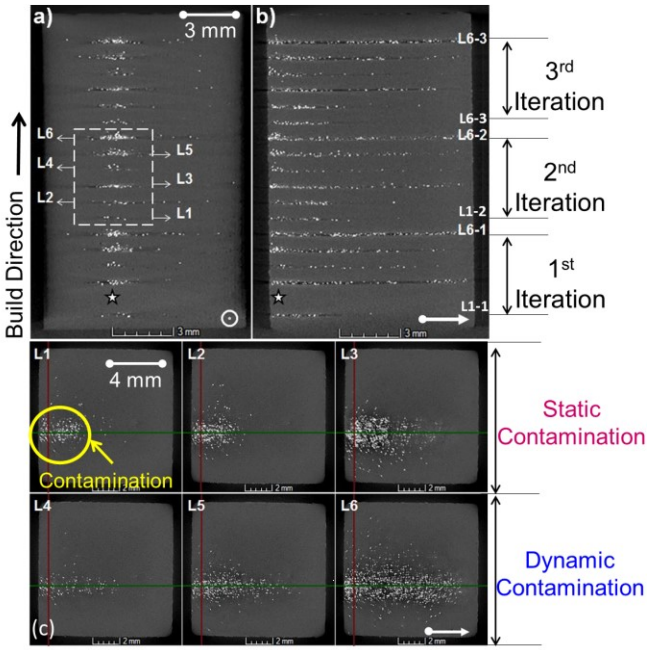

Figure 9: The cross sectional XCT views of the Inconel 625 specimen contaminated by the tungsten powder particles, a) vertical cross section normal to the recoating direction (cutting plane A-A, Y-Z direction), b) vertical cross section along the recoating direction (cutting plane B-B, X-Z direction) c) horizontal cross section (cutting plane C-C, X-Y direction). Due to procedural lapses in the XCT process the second contamination level in the first iteration (L2-1) was missed.

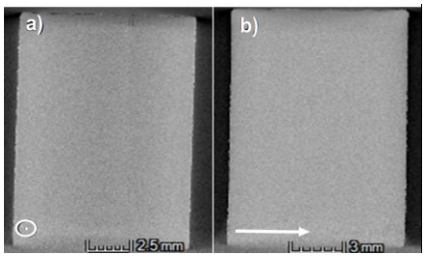

Figure 10: The cross sectional views of the Inconel 625 specimen contaminated by the Aluminum powder particles, a) vertical cross section normal to the recoating direction (cutting plane A-A, Y-Z direction), b) vertical cross section along the recoating direction (cutting plane B-B, X-Z direction). The contaminant particles are not evident within the aluminum matrix.

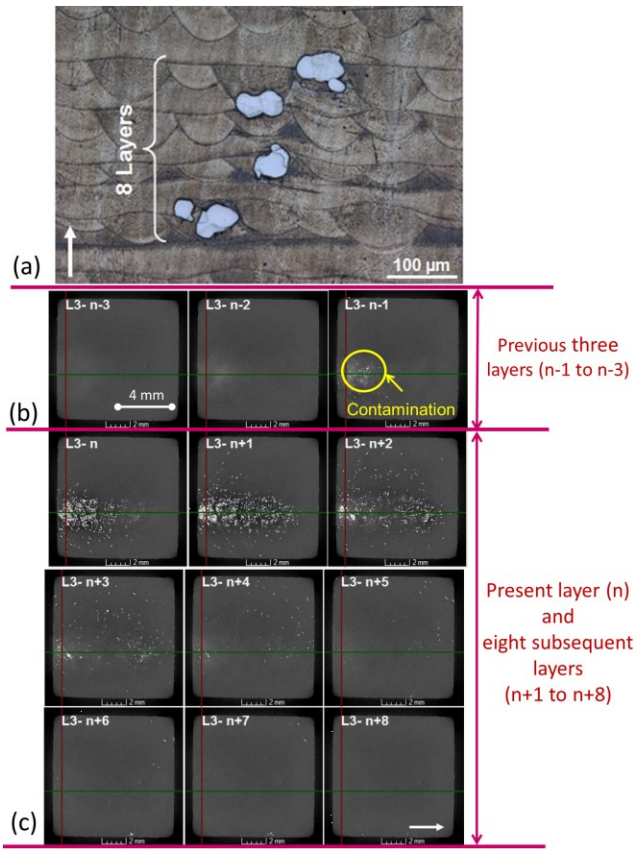

Figure 11: (a)The optical micrograph of the Inconel 625 specimen contaminated with tungsten particles observed over 8 layers. (b)(c) XCT images in the horizontal plane section (cutting plane C-C, X-Y direction) for the L_3 severity level shows that trace tungsten particles persist over eight subsequent layers and penetrate through three preceding layers.

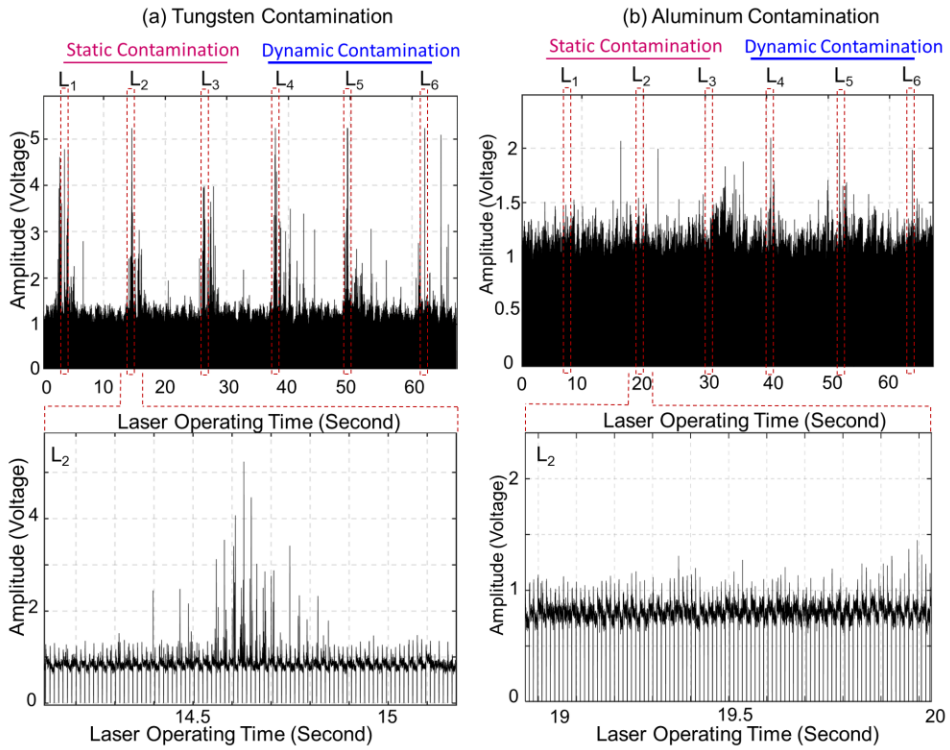

Figure 12: (top row) The photodetector signal associated with the six level of (a) Tungsten contamination and (b) Aluminum contamination in Inconel 625. (bottom row) The second contamination level (L_2) is magnified and the signal corresponding to tungsten contamination has clear spikes compared to aluminum.

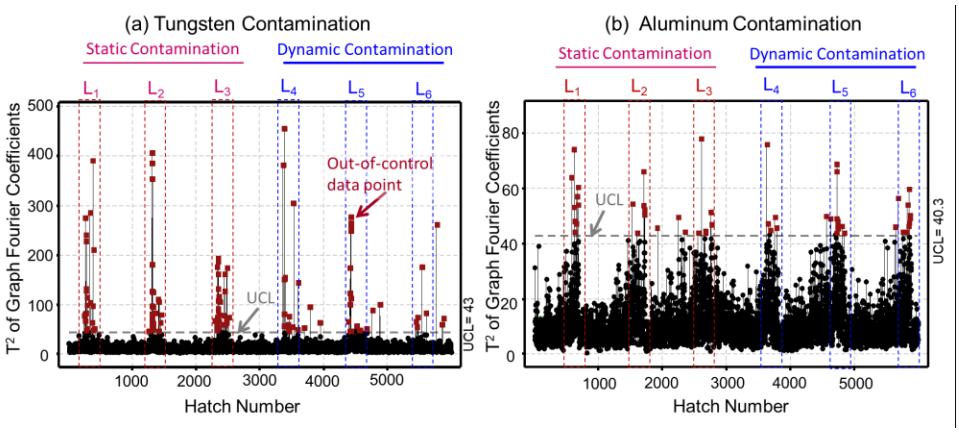

Figure 13: The Phase 1 spectral Hotelling T^2 control chart related to six levels of contamination for (a) Tungsten and (b) Aluminum contamination, wherein the control limits are fixed.

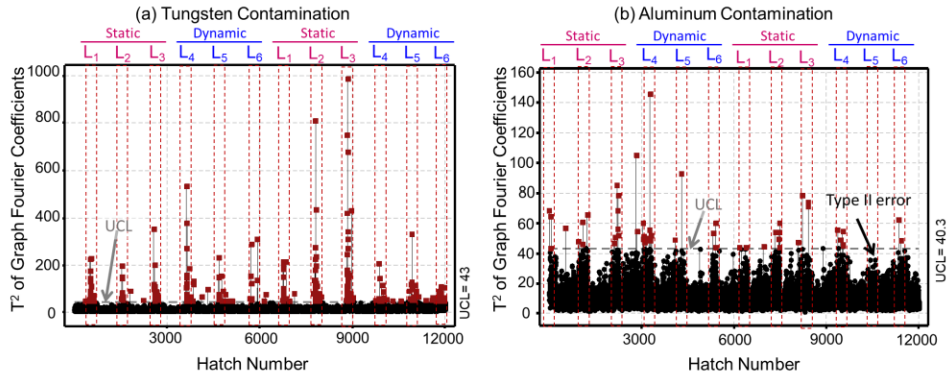

Figure 14: The Phase 2 spectral Hotelling T^2 control chart applied to two replications of the data for the related to the remaining two iterations, for each of the six levels of contamination for (a) tungsten and (b) aluminum contamination. Note that the dynamic contamination case L_5 for aluminum is not detected, indicating a Type II statistical error.

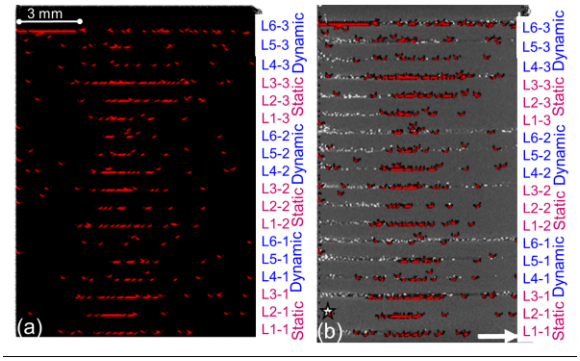

Figure 15: (a) The T^2 values of the spectral graph Fourier coefficients are color coded, red indicates out-of-control (contaminated) hatches, and black indicates in-control hatches. These T^2 values are plotted along the X-Z plane of the part, since the position of each hatch is known. (b) The spectral graph T^2 values are overlaid upon the XCT scan to demarcate the near one-to-one correspondence between the two.